Computations and Measurements of the Magnetic Polarizability Tensor Characterisation of Highly Conducting and Magnetic Objects

J. Elgy[†], P. D. Ledger[†], J. L. Davidson[‡], T. Özdeğer[‡], A. J. Peyton[‡]

[†]School of Computer Science and Mathematics, Keele University

[‡]Electrical and Electronic Engineering Department, The University of Manchester

Corresponding author: p.d.ledger@keele.ac.uk

August 13, 2023

Abstract

Purpose:
The ability to characterise highly conducting objects, that may also be highly magnetic, by the complex symmetric rank–2 magnetic polarizability tensor (MPT) is important for metal detection applications including discriminating between threat and non-threat objects in security screening, identifying unexploded anti-personnel landmines and ordnance and identifying metals of high commercial value in scrap sorting. Many everyday non-threat items have both a large electrical conductivity and a magnetic behaviour, which, for sufficiently weak fields and the frequencies of interest, can be modelled by a high relative magnetic permeability.

Design/methodology/approach:
The numerical simulation of the MPT for everyday non-threat highly conducting magnetic objects over a broad range of frequencies is challenging due to the resulting thin skin depths. We address this by employing higher order edge finite element discretisations based on unstructured meshes of tetrahedral elements with the addition of thin layers of prismatic elements. Furthermore, computer aided design (CAD) geometrical models of the non-threat and threat object are often not available and, instead, we extract the geometrical features of an object from an imaging procedure.

Findings:
We obtain accurate numerical MPT characterisations that are in close agreement with experimental measurements for realistic physical objects. Our assessment of uncertainty shows the impact of geometrical and material parameter uncertainties on our computational results.

Originality:
We present novel computations and measurements of MPT characterisations of realistic objects made of magnetic materials. A novel assessment of uncertainty in our numerical predictions of MPT characterisations for uncertain geometry and material parameters is included.

Keywords: Metal detection; eddy current; electromagnetic induction spectroscopy; magnetic polarizability tensor; object characterisation.

Article classification: Research paper.

1 Introduction

The rank–2 magnetic polarizbility tensor (MPT), which has a solid mathematical foundation and important real-world applications, has been shown to provide a useful economic characterisation of conducting objects for metal detection. Important applications include the discrimination between threat and non-threat objects in walk through metal detectors (e.g. Marsh et al. (2013, 2014), Makkonen et al. (2014, 2015), Davidson et al. (2023)), identifying anti-personnel landmines and unexploded ordnance from background metallic clutter in demining operations in post war countries and areas, in order to allow the land to be returned safely for civilian use (e.g. Abdel-Rehim et al. (2016), Özdeğer, Ledger & Peyton (2022), Elgy & Ledger (2023a)), identifying metal fragments in food and pharmaceutical production lines (e.g. Zhao et al. (2016, 2014)), and identifying metals of high commercial value in scrap sorting (e.g. Williams et al.

(2023), O'Toole et al. (2018)), where rapid differentiation between metallic materials is important from both a cost and an environmental perspective. For these applications, there is also considerable interest in characterising complex geometrical objects that contain both magnetic and non-magnetic metals. The term magnetic covers a broad range of physical phenomena, but for the purpose of this paper, we refer to a metallic material that displays an incremental relative magnetic permeability, μ_r, significantly greater than unity (so that $\mu_r > 1.5$, but often significantly larger). Non-magnetic metals are further classified as either paramagnetic (e.g. aluminium) if they have a relative magnetic permeability μ_r just larger than one, or diamagnetic (e.g. copper), if $\mu_r = 1$ or μ_r is just less than one (Hayt & Buck 2011)[pg 244-252]. This paper addresses the computation and measurement of MPT characterisations of objects made of magnetic metallic materials.

The mathematical theory for characterising conducting objects by MPTs is now well established and explicit formulae have been derived for the calculation of their coefficients (Ammari et al. 2014, Ledger & Lionheart 2015, Ledger et al. 2019) where it is known that the coefficients of the MPT are complex, symmetric, and independent of an object's position. There are considerable benefits to exploiting the MPT's spectral signature (Ledger & Lionheart 2020) (the variation of the MPT coefficients as a function of exciting frequency) compared to characterising an object by an MPT at a fixed frequency, which only characterises the object's shape and material parameters up to the best fitting ellipsoid. Improved object characterisations can also be obtained by using high order generalised magnetic polarizability tensors (GMPT) (Ledger & Lionheart 2018b, Özdeğer, Ledger, Lionheart & Peyton 2022), which provide additional information about the object. These results focus on the situation where an object is made of one or more materials, each with a linear constitutive relationship $\boldsymbol{B} = \mu_0\mu_r\boldsymbol{H}$ between the magnetic flux density $\boldsymbol{B}$ and the magnetic field strength $\boldsymbol{H}$ with μ_0 being the magnetic permeability of free space. In the case of magnetic materials, the magnetisation $\boldsymbol{M}$ also plays an important role, however, provided the fields are sufficiently weak and the material displays an essentially linear response, which is also taken to be isotropic, the constitutive relationship between $\boldsymbol{B}$ and $\boldsymbol{H}$ can be simplified to $\boldsymbol{B} = \mu_0\mu_r\boldsymbol{H}$, and while $\mu_r = \mu_r(\boldsymbol{B})$ in general, for fields where $|\boldsymbol{B}| < 1$ mT and the frequencies currently employed in metal detection, $\mu_r \gg 1$ can be regarded as a high constant relative magnetic permeability for magnetic materials (Landau et al. 1984)[pg. 200], which we will assume throughout.

Computational procedures based on the finite element method with a high order edge element ($\boldsymbol{H}$(curl) conforming) discretisation have been described for calculating the MPT characterisation of conducting objects (Ledger & Lionheart 2015). In addition, an efficient procedure for computing the MPT spectral signature object characterisation based on a reduced order model approach, using proper orthogonal decomposition (POD), has been developed (Wilson & Ledger 2021) and extended to higher dimensional parameter spaces (Elgy & Ledger 2023b). Dictionaries of MPT spectral signature characterisations of threat and non-threat objects have been developed (Ledger et al. 2021) and used as a basis for machine learning classifiers (Ledger et al. 2022) to distinguish between threat and non-threat objects using simulated data.

Accurate apparatus for measuring MPT spectral signatures has been developed for symmetrical (Özdeğer et al. 2021) and non-symmetrical objects (Özdeğer et al. 2023) and the measured MPT coefficients have been found to be in excellent agreement with the simulated MPT coefficients for the same object geometry and for material parameters chosen according to the metal in the samples. This apparatus has also been adapted to enable the measurement of GMPT coefficients (Özdeğer, Ledger, Lionheart & Peyton 2022), where excellent agreement between the measured and computed coefficients has also been obtained.

Previous work has focused on computing and measuring conducting objects, which are non-magnetic with $\mu_r = 1$ or μ_r close to unity. In this work, we wish to focus attention on the MPT characterisation of objects that are made of materials that are not only highly conducting, but also have high μ_r (such as nickel or steel). Such materials develop thin skin depths at higher frequencies, which make their characterisation more challenging to compute compared to objects with $\mu_r \approx 1$. In addition, we wish to consider the characterisation of objects with complex geometries. In Ledger et al. (2021), the computation of the MPT characterisation begins with setting up geometric models of objects by combining simple geometric primitives. However, this approach becomes increasingly complicated when complex geometries are involved and, in such situations, using a computer aided design (CAD) model, if one is available, is preferable. Nevertheless there are also many important threat and non-threat objects where CAD models are not readily available. These limitations are addressed through the main novelties of the work, which are:

1. Obtaining MPT characterisations of objects made of materials that are highly conducting and have high μ_r.

2. Accurately resolving thin skin depth effects associated with high μ_r and higher frequencies by applying the open source `NGSolve` finite element library (Schöberl 2014, Zaglmayr 2006, Schöberl 1997), using

enrichment of the element order and the construction of boundary layer meshes.

3. Computing MPT characterisations of realistic complex shapes where an exact geometry is not available by extracting geometric details from imaging of objects.

4. Understanding the uncertainty in the MPT characterisation of an object when its shape and material parameters are uncertain.

5. Accurate reproducibility of MPT measurements for complex physical objects with inhomogeneous materials.

The material presented in the paper is organised as follows: In Section 2 we recall the eddy current mathematical model that is appropriate for the metal detection problem, summarise previous results that estimate the eddy current modelling error and recall the object characterisation using the MPT. Then, in Section 3, we set out the computational procedure for computing the MPT characterisation including the description of how objects without a CAD description can be imaged to extract their geometry. Section 4 briefly recalls the apparatus and approach used for measuring MPT object characterisations. In Section 5 we present a series of results of object characterisations where measurements and simulations are compared, which includes objects that are magnetic and objects that do not have a CAD description. The paper closes with some concluding remarks in Section 6.

2 Mathematical Model

The eddy current model is a low–frequency approximation to the time harmonic Maxwell system where the displacement currents are neglected. As described in Section 1, assuming isotropic magnetic materials described by a linear constitutive relationship between the magnetic flux density and the magnetic field strength for sufficiently weak fields, it is given by

$$\nabla \times \boldsymbol{E}_\alpha = \mathrm{i}\omega\mu_\alpha \boldsymbol{H}_\alpha, \tag{1a}$$

$$\nabla \times \boldsymbol{H}_\alpha = \sigma_\alpha \boldsymbol{E}_\alpha + \boldsymbol{J}_0, \tag{1b}$$

where $\boldsymbol{E}_\alpha$, $\boldsymbol{H}_\alpha$ are the electric and magnetic interaction fields, $\boldsymbol{J}_0$ is the external current source, ω is the angular frequency, μ_α is the position dependent magnetic permeability and σ_α is the position dependent electrical conductivity. Considering the situation of a single conductor B_α in a non–conducting region, then,

$$\sigma_\alpha = \left\{ \begin{array}{ll} \sigma_* & \text{in } B_\alpha \\ 0 & \text{in } B_\alpha^c = \mathbb{R}^3 \backslash \overline{B_\alpha} \end{array} \right. , \qquad \mu_\alpha = \left\{ \begin{array}{ll} \mu_* & \text{in } B_\alpha \\ \mu_0 & \text{in } B_\alpha^c \end{array} \right. ,$$

where $\mu_0 = 4\pi \times 10^{-7}$ H/m is the permeability of free space and we assume σ_* and μ_* are independent of ω and $\boldsymbol{J}_0$ only has support in B_α^c and is away from B_α. In the following, we assume that B_α can be described as $B_\alpha := \alpha B + \boldsymbol{z}$, where α describes the object's size, B is a unit-sized object with the same shape as B_α, but centered at the origin, and $\boldsymbol{z}$ is the translation from the origin. We also introduce $\mu_r := \mu_*/\mu_0$ as the relative magnetic permeability.

2.1 Estimating the eddy current error

The eddy current model described by (1) is often quoted as being valid when σ_* is large and ω is small, but α, μ_r and the topology of B also play an important role. Some classical texts (e.g. Wait (1951)) state that the eddy current model applies when

$$\alpha \ll \lambda_0, \tag{2}$$

where λ_0 is the free space wavelength obtained from $k_0 = \omega\sqrt{\epsilon_0\mu_0} = 2\pi/\lambda_0$ and $\epsilon_0 = 8.854 \times 10^{-12}$ F/m is the electrical permittivity of the background, but this does not take into account the topology of the object or its material parameters. Commonly, many engineering text state that the eddy current model applies if the quasi-static approximation applies and the conductivity of the object is high, i.e.

$$\alpha \ll \lambda, \qquad \text{and} \qquad \omega\epsilon_* \ll \sigma_*, \tag{3}$$

where ϵ_* is the permittivity of B_α, but this does not take in to account the topology of B_α. Note that in a conductor, the wavenumber is complex

$$k = k' + \mathrm{i}k'' = \sqrt{\omega^2\epsilon_*\mu_* + \mathrm{i}\mu_*\sigma_*\omega}, \tag{4}$$

3

and $\lambda_C = 2\pi/k'$, while the imaginary part k'' relates to the depth of penetration of the fields inside the conductor measured by the skin depth (the depth to which the fields decay to $1/e$ of their surface value) given by Balanis (2012)

$$\delta := \frac{1}{\sqrt{\frac{\omega^2 \mu_* \epsilon_*}{2} \sqrt{1 + \left(\frac{\sigma_*}{\omega \epsilon_*}\right)^2} - 1}} \approx \sqrt{\frac{2}{\sigma_* \omega \mu_*}}, \tag{5}$$

where the above approximation certainly holds in the eddy current regime, as $\epsilon_* \approx \epsilon_0$, $\sigma_* \approx 10^6$ S/m and ω is typically in the 0.1 kHz-10 kHz range for metal detection, although we would also expect this to be true hold for much higher frequencies too.

Ammari et al. (2000) have rigorously shown that the solutions to (1) are first or second order accurate for small frequencies depending on the topology of B_α. Building on this, and noting that for highly conducting objects, $\lambda_C \ll \lambda_0$ and λ_C are also influenced by μ_*, Schmidt et al. (2008) propose that the eddy current model hold if

$$C_1 \epsilon_* \mu_* \omega^2 \alpha^2 \ll 1 \qquad \text{and} \qquad C_2 \frac{\omega \epsilon_*}{\sigma_*} \ll 1, \tag{6}$$

which, for moderate C_1, C_2, is approximately equivalent to (3). They also provide a procedure for computing C_1, C_2, depending on the object's topology, which reduce to moderate values for simply connected objects. This approach has been applied in Ledger et al. (2021) to determine where the eddy current approximation breaks down. In this work, for the object geometries and material parameters considered, we limit ourselves to frequencies such that the eddy current model holds in the sense of (6).

2.2 Object characterisation using the MPT

Our interest lies in characterising hidden conducting magnetic objects when the eddy current approximation of the Maxwell system applies. Given orthonormal coordinate basis vectors $\mathbf{e}_i$, $i = 1, 2, 3$, and using Einstein summation convention, the complex symmetric rank–2 MPT

$$\mathcal{M} = (\mathcal{M})_{ij} \boldsymbol{e}_i \otimes \boldsymbol{e}_j, \tag{7}$$

which is a function of B, α, μ_r, σ_* and ω, but independent of object position, has been shown to provide object characterisation information in the leading order term of an asymptotic expansion of the perturbed magnetic field for small objects in the form

$$(\boldsymbol{H}_\alpha - \boldsymbol{H}_0)(\boldsymbol{x})_i = (\boldsymbol{D}_x^2 G(\boldsymbol{x}, \boldsymbol{z}))_{ij} (\mathcal{M})_{jk} (\boldsymbol{H}_0(\boldsymbol{z}))_k + (\boldsymbol{R}(\boldsymbol{x}))_i. \tag{8}$$

In the above, $G(\boldsymbol{x}, \boldsymbol{z}) = 1/(4\pi|\boldsymbol{x} - \boldsymbol{z}|)$ denotes the free space Green's function, $\boldsymbol{H}_0(\boldsymbol{z})$ the background magnetic field at the position of the object and $\boldsymbol{R}(\boldsymbol{x})$ a residual term with known form (Ledger & Lionheart 2015, Ledger et al. 2019, Ledger & Lionheart 2018a, 2020). Furthermore, we have derived explicit formulae for computing

$$\text{Re}\left(((\mathcal{M}(\alpha B, \omega, \sigma_*, \mu_r))_{ij}\right) = (\tilde{\mathcal{R}}(\alpha B, \omega, \sigma_*, \mu_r))_{ij} = (\mathcal{N}^0(\alpha B, \mu_r))_{ij} + (\mathcal{R}(\alpha B, \omega, \sigma_*, \mu_r))_{ij}, \tag{9a}$$

$$\text{Im}\left(((\mathcal{M}(\alpha B, \omega, \sigma_*, \mu_r))_{ij}\right) = (\mathcal{I}(\alpha B, \omega, \sigma_*, \mu_r))_{ij}, \tag{9b}$$

which are based on post-processing the solution of vectorial transmission problems for $\boldsymbol{\theta}_i^{(1)}$ and $\boldsymbol{\theta}_i^{(0)}$ (Ledger & Lionheart 2020). In addition, we refer to the aforementioned references for additional properties of the MPT.

Arranging the coefficients of $\tilde{\mathcal{R}}$ and $\mathcal{I}$ as real symmetric 3×3 matrices, we observe that they each admit real eigenvalues. We choose to order the eigenvalues by their multiplicity (ordering those with the highest multiplicity first) and treat the eigenvalues of $\tilde{\mathcal{R}}$ and $\mathcal{I}$ separately. In cases where all three eigenvalues are unique, then they are sorted in ascending order.

3 Computational Procedure

An efficient procedure for computing the MPT spectral signature of a conducting object has been proposed in Wilson & Ledger (2021) and a revised and improved implementation by Elgy & Ledger (2023b) is in the updated `MPT-Calculator`[1] (InitialRelease branch), using version 6.2.2204 of the higher order `NGSolve` finite

---

[1] An updated version of MPT-Calculator is available at `https://github.com/MPT-Calculator/MPT-Calculator`

library (*NGSolve* n.d., Schöberl 2014, Zaglmayr 2006), and will be used throughout the work to generate the numerical results. The approach computes discrete approximations to $\boldsymbol{\theta}_i^{(1)}$ and $\boldsymbol{\theta}_i^{(0)}$ for a small number of sets of problem parameters using `NGSolve` with a $\boldsymbol{H}(\text{curl})$ conforming discretisation on unstructured (tetrahedral) grids (Schöberl & Zaglmayr 2005, *NGSolve* n.d., Schöberl 2014, Zaglmayr 2006) and the `Netgen` mesher. These N solutions are called the representative full-order model solution snapshots. A proper orthogonal decomposition approach using projection (PODP) is then applied to predict the discrete approximations to $\boldsymbol{\theta}_i^{(1)}$ and $\boldsymbol{\theta}_i^{(0)}$ at other problem parameters. Note that this requires that the same mesh and order of elements are used for all sets of problem parameters considered. The MPT coefficients in (9) are then found by post-processing leading to the MPT spectral signature characterisations of different objects.

This approach has been successfully applied to characterise a range of threat and non-threat objects in Ledger et al. (2021) and then the resulting dictionary has been used to develop an efficient machine learning approach for object classification in Ledger et al. (2022). However, the characterisations considered were limited to non-magnetic objects with $\mu_r = 1$ or $\mu_r \approx 1$ and to object geometries that were constructed from combining `Netgen` primitives. For magnetic objects with $\mu_r \gg 1$ the skin depth δ becomes very small as the frequency is increased and, as a result, very large field gradients are experienced close to the surface of the conductor resulting in a boundary layer effect that is common in fluid dynamics and mechanical problems. Using traditional h–refinement of the grid to capture these field gradients leads to large meshes of elements and using p–refinement alone is sub–optimal as it best suited to capturing smooth solutions rather than solutions with sharp gradients. Furthermore, complex object geometries present additional challenges as they cannot easily be built from simple geometric primitives in the `Netgen` mesher. We set out below how these challenges are overcome.

3.1 Boundary layer meshes

To resolve the thin skin depth, the concept of anisotropic boundary layer meshes combined with p–refinement can be applied to accurately capture the high field gradients. For related problems involving a singularly perturbed elliptic problem, the use of such meshes has been shown to result in exponential convergence of the numerical solution (Schwab & Suri 1996). Hence, to improve the rate of convergence of the numerical solutions to $\boldsymbol{\theta}_i^{(1)}$, we include layers of prismatic elements to achieve the anisotropic refinement close to the surface of B. The introduction of such elements increases the number of degrees of freedom by a small amount, but also considerably improves the resolution of $\boldsymbol{\theta}_i^{(1)}$ in the direction that is normal to the surface of B for thin skin depths. The required $\boldsymbol{H}(\text{curl})$ conforming basis functions for prismatic elements are available in the `NGSolve` library and so their introduction is straight forward. In particular, we use the Open Cascade Technology in `NGSolve` to define geometries and use their `Netgen` mesher to generate hybrid meshes of tetrahedra and prisms. For further details we refer to the `NGSolve` documentation (*NGSolve* n.d.). An illustration of a typical mesh including a prismatic boundary layer is shown in Figure 1.
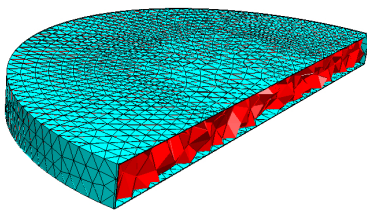

Figure 1: British conducting magnetic 1p coin (post-1992): illustration of a cut through the unstructured tetrahedral mesh inside the object showing the tetrahedra (red) and prisms (cyan).

We provide numerical examples to illustrate the improvements in accuracy obtained by including prismatic elements in combination with p–refinement for objects with magnetic materials and thin skin depths in Section 5.1.

3.2 Obtaining geometric information of complex objects

For simple objects, geometric primitives in `Netgen` can be combined to create object descriptions, as has been illustrated in Ledger et al. (2021). However, for complex objects, this becomes increasingly complicated and, as CAD descriptions are not always readily available, an alternative approach is needed. In this work, for small objects with overall dimensions contained in the bounding box $[0, 0.03]^3$ m^3 to

Figure 2: Demonstrative photo of `EinScan` experimental setup and measurement procedure.

$[0, 0.2]^3$ m^3 that cannot be easily constructed from combining `Netgen` geometric primitives (Schöberl 1997), we will use the Shining-3D `EinScan-SE` imaging tool and their `EXScan-S` (version 3.1.2.0) software (EinScan n.d.) for producing geometry descriptions. Note that while the `EXScan-S` software and the Shining-3D `EinScan-SE` imaging tool can also be used to produce textured images of 3D objects this is not our goal as we are only interested in capturing the geometrical information of the objects. To image objects, they are placed on a turntable and and their geometric features are captured using structured light scanning. The details of the imaging procedure are:

1. Objects are prepared with a thin layer of matt-grey primer to improve their contrast and make them matt (rather than shiny) in appearance to aid with the imaging.

2. Images of the object were constructed by using non-textured scans under a full rotation split into $10°$ increments using the `EXScan-S` software. This was achieved by using a small amount of double sided tape to keep the object in an up-right position while the rotations were performed. In the case of objects with magnetic materials, the object was fixed using a small ($\approx 5 \times 10^{-3}$ m) spherical chrome magnet. Due to the small shiny nature of the magnet it does not appear in the resultant point cloud. An illustrative example is provided in Figure 2, where a small key is shown on the turntable. Effort was taken to ensure that the lighting was consistent throughout the measurement and the scanner was regularly re-calibrated to account for day-to-day changes in lighting. In all cases, the scanner was placed in front of a large white box. This was to remove depth features from clutter on the far wall. In addition, the white balance of the camera was adjusted such that the box was over exposed but the object was not. In most lighting conditions, this was half the available range. For thick objects where one dimension is not negligible compared to the others and where the point cloud is nonexistent or insufficient to describe the geometry via visual inspection (from experience, this corresponds to a minimum dimension greater than approximately 4×10^{-3} m), we rotate the object $90°$ around the horizontal axis, illustrated in Figure 3, and remeasure under the same settings. The two point clouds then undergo feature based co-registration using the `ExScan-S` software. Three features are chosen to be prominent and corresponding to dense areas of the point cloud for both measurements. For thin objects whose minimum dimension is less than 2×10^{-3} m, the scan does not result in a dense point cloud regardless of orientation. In such a scenario, rotating the object does not provide significant additional information.

3. Using the `EXScan-S` software the point cloud was downsampled to a quasi-uniform distribution. In addition, minor issues and undesired imaging artefacts were removed in this software. While the downsampling of the point cloud results in a coarser resolution of the geometric features (as is illustrated in Figure 12), the loss of these geometrical features is not critical to the MPT characterisation of an object and allows us to construct a coarser finite element discretisation, reducing the computational cost of our simulations.

4. The resulting output from the `EXScan-S` software is a point cloud description of the object saved as a `.stl` format. Where necessary, meshes were then manually adjusted to remove unwanted interior faces and fix mesh discontinuities. This involves using 3D modelling software (we used Autodesk Meshmixer version 3.5.474) to remodel the object as a contiguous watertight mesh. We then perform a quasi-uniform isoparametric remeshing of the surface to remove any degenerate or intersecting mesh faces using MeshLab (version 2022.02).
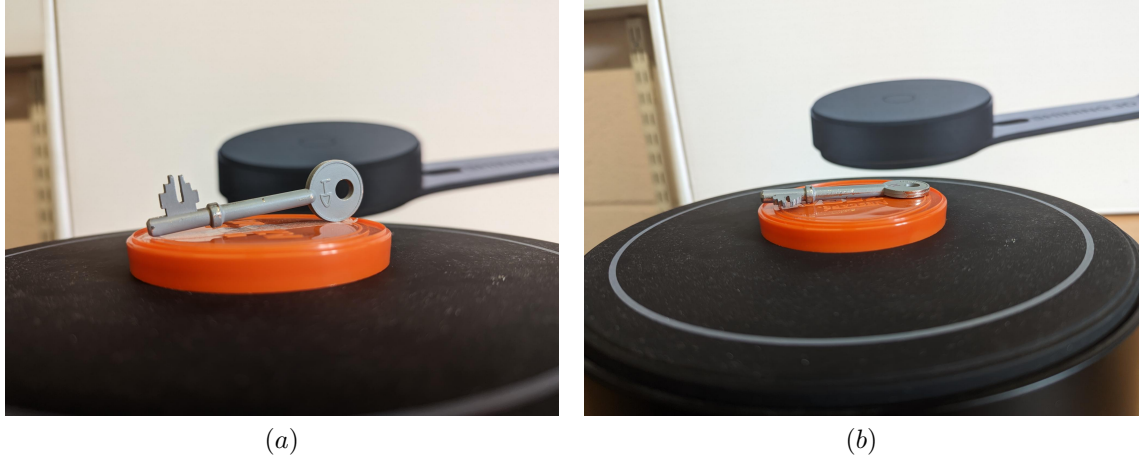
Figure 3: Example of the two different orientations used in step 2 of the imaging procedure showing: (a) vertical orientation, and (b) horizontal orientation.

5. The point cloud was converted to a quasi-uniform mesh and saved as a `.step` format using the Maya Autodesk `Fusion-360` CAD package (version 2.0.1413) (Autodesk n.d.). The conversion to the `.step` format was performed in a faceted manner where no smoothing or pointwise interpolation occurs. The `.step` format file therefore consists of multiple faces.

6. An unstructured mesh of tetrahedra describing the object and the region out to a truncation boundary placed sufficiently far from the object is created with `Netgen` using `OCC-geometry` and importing the `.step` file. At this stage, we also centre the object and, if appropriate, introduce additional prismatic boundary layer elements to help approximate the high field gradients in the thin skin depths for highly magnetic objects.

4 Measurement Procedure

MPT measurements were acquired using a bespoke instrument comprising of three main parts, a multi-coil arrangement, custom electronics, and control software on a PC. For the measurements reported in this work, the system was operated over a frequency range from 119.25 Hz to 9.54×10^4 Hz (749.26 rad/s to 5.99×10^5 rad/s). The control software sets transmit control signals, e.g. frequency, signal amplitudes and digital signal processing (DSP) settings to a dedicated microcontroller (Red Pitaya `STEMlab` 125-14). The microcontroller generates the software-set excitation signals and sends to dedicated power amplifiers (Analog Devices LT 1210) to produce upto 64 V peak-to-peak sine wave limited to 10 A to the transmit coil. Measurement signals from the receive coils are amplified and filtered by custom-made electronics controlled via the DSP of the microcontroller. Subsequent signal averaging of the acquired measurements were performed in the control software prior to MPT inversion. Full details of the coil arrangement, bespoke electronics and data acquisition are detailed in Özdeğer et al. (2021) and Özdeğer et al. (2023). Measurements employed the use of a bespoke Target Orientation Manipulator (TOM) based on a truncated Icosahedron (tI) enabling the test object rotation in three-dimensional space. The TOM is hollow and sectioned in two separable halves and is constructed from 3D printed polylactic acid (PLA) filament and has a point-to-point diameter of 0.15 m and a 0.01 m wall thickness. Each face of the TOM utilises a keyed hole in the middle. These are used to place the faces on a custom-made table with a keyed seat within the coil arrangement. This ensures control of the horizontal position of the target and thereby keeps rotation around the vertical axis fixed for consistency. The use of the tI method has been fully described in Özdeğer et al. (2023) and enables non-symmetrical target objects to be characterised. The tested objects presented in this work were firmly secured in the centre of the TOM using adhesive tape. All measurements were carried out in a temperature and humidity-controlled environment after an instrument warm-up period of a least 30 minutes to minimise thermal drift within the system electronics and coil arrangement. In order to quantify measurement precision and short-term measurement stability, a set of repeated coin measurements were taken, which are discussed further in Section 5.2.

An illustrative photograph of the measurement system is shown in Figure 4, where the coil array, TOM, bespoke system electronics including transmit and receive stages along with a dedicated microcontroller, and an oscilloscope (used for observation of the transmit signal) are shown.
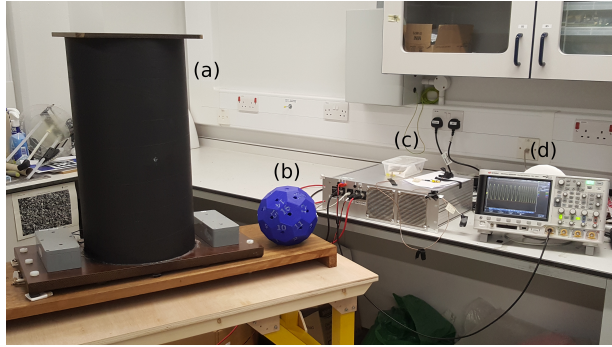
Figure 4: MPT measurement system showing (a) the coil array, (b) the TOM, (c) bespoke system electronics including transmit and receive stages along with dedicated microcontroller, and (d) an oscilloscope used for observation of the transmit signal.

5 Results

5.1 Sphere

An exact solution is available for the MPT characterisation of this object allowing us to investigate the accuracy of our approximate object characterisation scheme. We note that previous results have established that the approximate MPT spectral signature obtained from p–convergence of the full order model solution agrees well with the exact solution over a wide band of frequencies and non-magnetic material parameters (e.g. Wilson & Ledger (2021) shows comparisons for a sphere or radius $\alpha = 0.01$ m and material parameters $\sigma_* = 5.96 \times 10^6$ S/m, $\mu_r = 1.5$). Our interest in this paper is the ability to characterise magnetic materials, where $\mu_r \gg 1$, over a broad range of frequencies including those resulting in thin skin depths, which are more challenging to capture.

We first consider the approximation to the MPT spectral signature characterisation of a conducting magnetic sphere with radius $\alpha = 0.01$ m, conductivity $\sigma_* = 1 \times 10^6$ S/m and different relative permeabilities $\mu_r = 20, 40, 80$ for the frequency range $1 \times 10^1 \leqslant \omega \leqslant 1 \times 10^8$ rad/s. The results were obtained by considering a unit sized sphere B placed in a truncated domain of dimension $[-1000, 1000]^3$ units and discretised by an unstructured mesh of 21 424 tetrahedra. We consider $N = 13$ full-order model solution snapshots computed using different uniform orders of approximation $p = 0, 1, 2, 3, 4, 5$ at logarithmically spaced frequencies. We show the approximate solutions for $\lambda_1(\tilde{\mathcal{R}})$ and $\lambda_1(\mathcal{I})$ obtained using the POD based reduced order model with a POD tolerance of $TOL = 1 \times 10^{-6}$ in Figure 5. The behaviour for the other eigenvalues is similar. While increasing p does tend towards convergence of the numerical solution to the exact solution, we see that the maximum frequency for which we get good agreement reduces as μ_r increases. This is due to the smaller skin depths associated with higher μ_r and larger ω, which make the solution to the transmission problem for $\boldsymbol{\theta}_i^{(1)}$ more challenging to resolve. If a discretisation with $p > 5$ order elements were used, they would eventually tend to the exact solution over the complete frequency range considered, but this would be computationally prohibitive. Another alternative would be to use a locally refined mesh of tetrahedra with refinement targeted to just inside the surface of B, but, again, this would lead to a large increase in the number of degrees of freedom and require prohibitively large computational resources.

As an alternative, we consider the same conducting sphere, but instead consider POD solution where the full order model snapshot solutions were obtained using a discretisation consisting of 21 150 unstructured tetrahedra with the addition of 3 thin prismatic layers just inside the surface of B (1 449 prisms in total). The thicknesses of the layers were chosen as $1 \times 10^{-3}, 5 \times 10^{-3}$, and 5×10^{-2} units, respectively. Figure 6 shows the approximate solutions for $\lambda_1(\tilde{\mathcal{R}})$ and $\lambda_1(\mathcal{I})$ obtained using the POD settings as before and uniform orders of approximation $p = 0, 1, 2, 3, 4, 5$. In this figure, we observe rapid convergence of the numerical solution to the exact solution over the complete range of frequencies considered for the three cases of $\mu_r = 20, 40, 80$. In each case, $p = 2$ order elements already provides an accurate solution, which is far superior to $p = 5$ on a mesh of 21 424 tetrahedra and solutions for $p = 3$ and above are almost indistinguishable from each other on this scale.

To further demonstrate the advantages of combining p–refinement with prismatic layers, we compare the relative error $E = \|\mathcal{M}^{exact} - \mathcal{M}^{hp}\|_F / \|\mathcal{M}^{exact}\|_F$ using the Frobenious norm against $N_d^{1/3}$, where N_d is the number of degrees of freedom, in Figure 7, for the case of a conducting permeable and magnetic sphere of radius $\alpha = 0.01$ m, with conductivity $\sigma_* = 1 \times 10^6$ S/m, relative permeability $\mu_r = 20$, and frequency $\omega = 1 \times 10^6$ rad/s for p–refinement on three different meshes. Note that a straight line on this graph indicates exponential convergence and increased slope indicates superior convergence performance
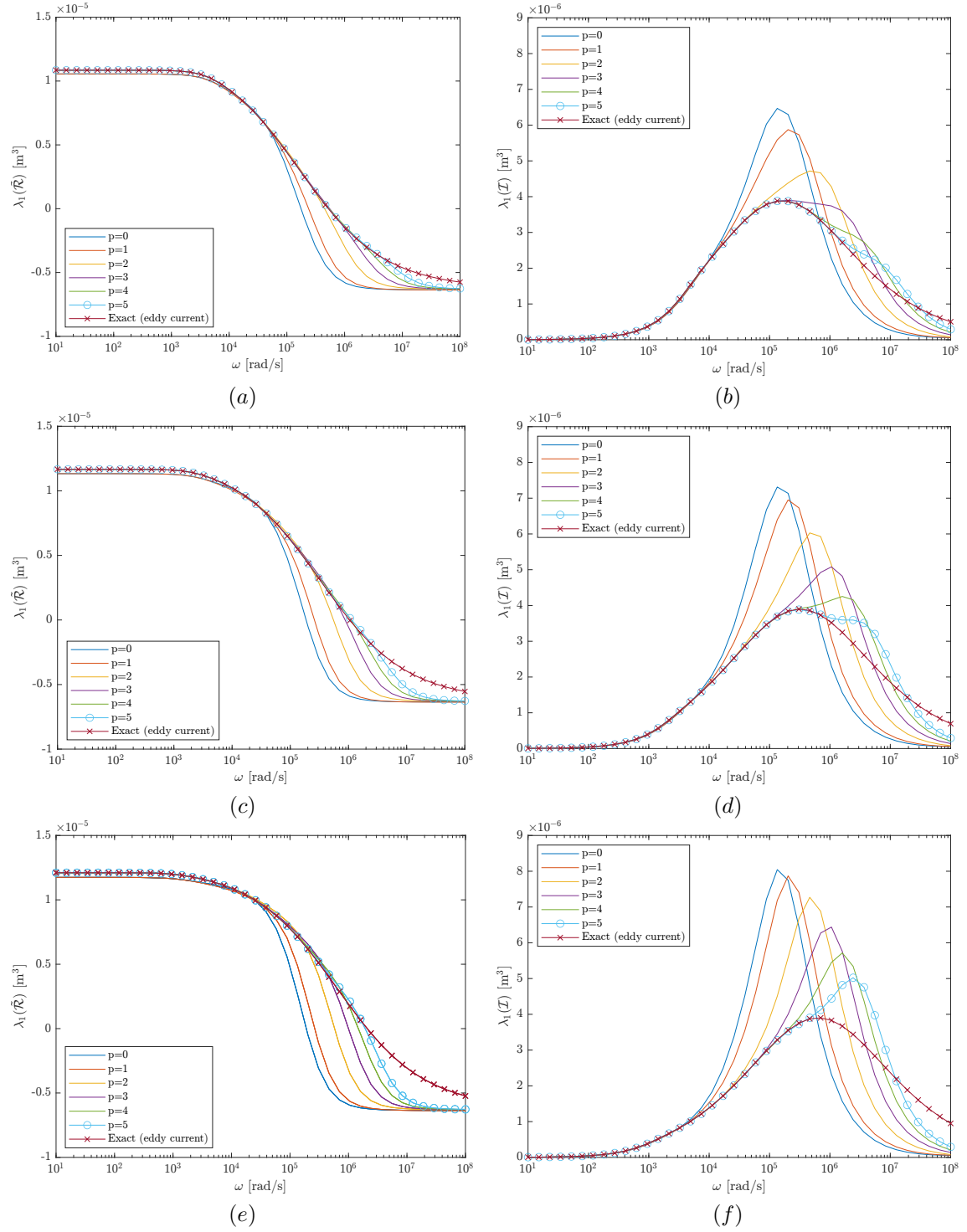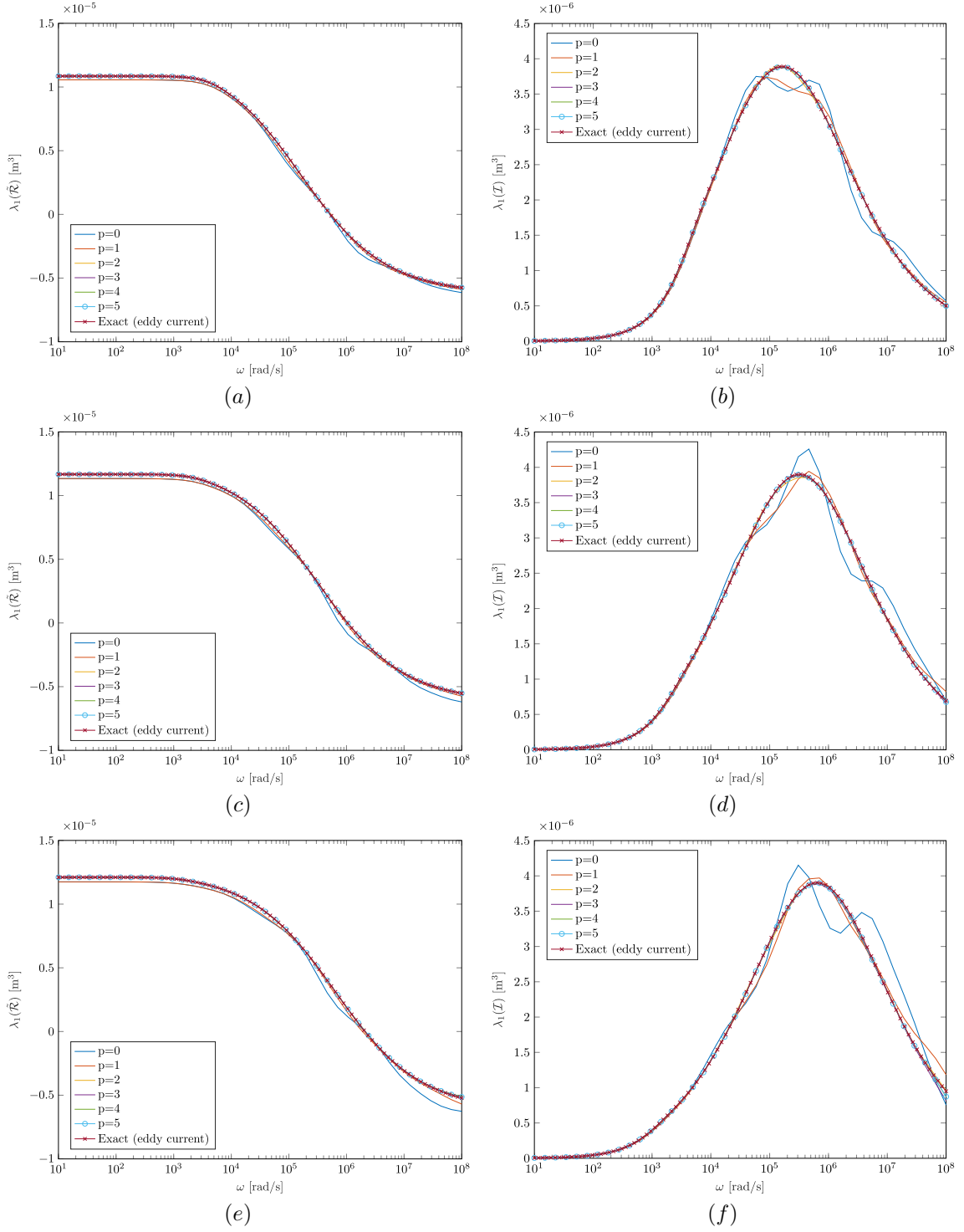
Figure 5: Conducting magnetic sphere with radius $\alpha = 0.01$ m, conductivity $\sigma_* = 1 \times 10^6$ S/m and relative magnetic permeabilities $\mu_r = 20, 40, 80$, showing convergence of the MPT spectral signatures to the exact solution using POD with full order model solution snapshots at logarithmically spaced frequencies using different uniform orders of approximation $p = 0, 1, 2, 3, 4, 5$ on an unstructured mesh of 21 424 tetrahedra: (a) $\lambda_1(\tilde{\mathcal{R}}(\alpha B, \omega, \sigma_*, \mu_r = 20))$, (b) $\lambda_1(\mathcal{I}(\alpha B, \omega, \sigma_*, \mu_r = 20))$, (c) $\lambda_1(\tilde{\mathcal{R}}(\alpha B, \omega, \sigma_*, \mu_r = 40))$, (d) $\lambda_1(\mathcal{I}(\alpha B, \omega, \sigma_*, \mu_r = 40))$, (e) $\lambda_1(\tilde{\mathcal{R}}(\alpha B, \omega, \sigma_*, \mu_r = 80))$ and (f) $\lambda_1(\mathcal{I}(\alpha B, \omega, \sigma_*, \mu_r = 80))$.

9

Figure 6: Conducting magnetic sphere with radius $\alpha = 0.01$ m, conductivity $\sigma_* = 1 \times 10^6$ S/m and relative magnetic permeabilities $\mu_r = 20, 40, 80$, showing convergence of the MPT spectral signatures to the exact solution using POD with full order model solution snapshots at logarithmically spaced frequencies using different uniform orders of approximation $p = 0, 1, 2, 3, 4, 5$ on an unstructured mesh of $21\,150$ tetrahedra with the addition of 3 prismatic layers comprising of $1\,449$ prisms in total: (a) $\lambda_1(\tilde{\mathcal{R}}(\alpha B, \omega, \sigma_*, \mu_r = 20))$, (b) $\lambda_1(\mathcal{I}(\alpha B, \omega, \sigma_*, \mu_r = 20))$, (c) $\lambda_1(\tilde{\mathcal{R}}(\alpha B, \omega, \sigma_*, \mu_r = 40))$, (d) $\lambda_1(\mathcal{I}(\alpha B, \omega, \sigma_*, \mu_r = 40))$, (e) $\lambda_1(\tilde{\mathcal{R}}(\alpha B, \omega, \sigma_*, \mu_r = 80))$ and (f) $\lambda_1(\mathcal{I}(\alpha B, \omega, \sigma_*, \mu_r = 80))$.

properties. We focus on $\omega = 1 \times 10^6$ rad/s as the error is visibly large for one of the approaches. We consider the purely tetrahedral mesh and hybrid mesh discussed above (Figures 5 and 6) as well as a hybrid mesh with 2 prismatic layers with thicknesses chosen according to a geometric progression (Elgy & Ledger 2023a), resulting in a mesh consisting of 21 151 tetrahedra and 1 275 prisms. The results show that
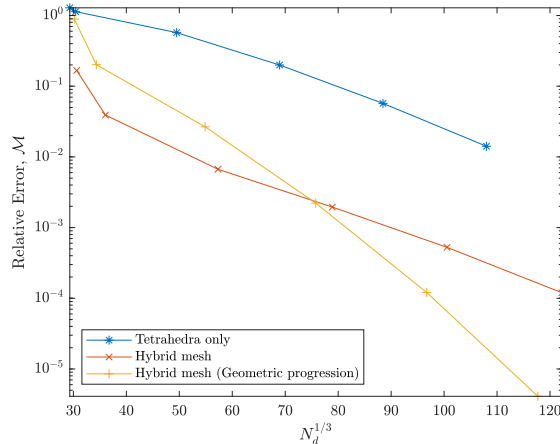

Figure 7: Conducting magnetic sphere with radius $\alpha = 0.01$ m, $\sigma_* = 1 \times 10^6$ S/m, and relative magnetic permeability $\mu_r = 20$ at a frequency $\omega = 1 \times 10^6$ rad/s. p–refinement, showing the error, E, for $p = 0, 1, 2, 3, 4, 5$ for three different meshes, the tetrahedral and non–geometric hybrid meshes used in Figures 5 and 6, respectively, and a hybrid mesh with a geometric structure.

with p–refinement both hybrid meshes out-perform p–refinement on the purely tetrahedral mesh, with the hybrid mesh using prismatic layers with thicknesses chosen according to a geometric progression giving the best performance. For further details on the theory of boundary layers and hp–refinement we refer to Schwab & Suri (1996) and for details on a simple practical approach for choosing the thickness of layers for magnetic materials with thin skin depths, such as those used in Figure 7, we refer to Elgy & Ledger (2023a). For the remainder of this work, we primarily consider objects where there is a thin metallic coating of known or assumed thickness and, in such cases, the thickness of the boundary layers are chosen accordingly.

5.2   Recent British coins

Building on the computed MPT characterisations of 1p (one penny), 2p (two pence), 5p (five pence), 10p (ten pence), 20p (twenty pence), 50p (fifty pence), £1, and £2 denominations of British coins presented in Ledger et al. (2021), we consider a larger range of British coins that are currently in circulation and include more recent changes to their compositions. In particular, to reduce the manufacturing costs, and to ensure that the costs of the metallic materials used for a denomination of coin do not exceed its face value, the amount of copper used in the lower denominations of British coins has been reduced and/or replaced by a lower cost metal with a thin coating or cladding. For example, in 1992, the 1p and 2p coins, which were originally 97% copper, 2.5% zinc and 0.5% tin, were replaced with a new composition comprising of a mild steel core (94% by volume) and a thin coating of copper (6% by volume) (Brunning 2014). Similarly, more recently minted 5p and 10p coins have a mild steel core with a nickel coating. The 20p, 50p, and £1 coins are non-circular and the £1 and £2 coins each consist of an annulus filled with a circular disc. Details of the composition of British coins currently in circulation is presented in Table 1, which includes coins whose composition is made from a solid material and also those with coatings. Importantly, this table only presents estimates of the conductivity and permeability in all cases, which, in some cases can vary considerably (e.g. mild steel and nickel, which we have chosen to model as $\sigma_* = 6 \times 10^6$ S/m, $\mu_r = 200$ and $\sigma_* = 1.45 \times 10^7$ S/m, $\mu_r = 100$, respectively). Similarly, the thickness of the coating for more recent 1p, 2p, 5p and 10p coins is unknown and are estimates are based on Brunning (2014). We will also consider the effects of these uncertainties on our simulations in Section 5.2.1.

To compute the MPT spectral signature characterisations of the coated 1p (post-1992), 2p (post-1992), 5p (post-2011) and 10p (post-2011) coins we consider discretisations of the non-dimensional coin B, centered at the origin with dimensions set according to those in Ledger et al. (2021) and $\alpha = 1 \times 10^{-3}$ m. We truncate the otherwise unbounded domain with a truncation boundary in the form of a cylinder with height and radius 1000 units resulting in an unstructured tetrahedral mesh with 89 976, 134 874, 82 004 and 101 777 tetrahedra, respectively, and the addition of a single prismatic layer to model the coating

Coin mint date	Modelled shape	Total diameter [10^{-3} m]	Total thickness [10^{-3} m]	Coating thickness [10^{-3} m]	Composition	Relative permeability (μ_r)	Conductivity (σ_*) [S/m]
1p (1971-1992)	Circular disc	20.3	1.52	n/a	97% Copper, 2.5% zinc and 0.5% tin	1	4.03×10^7
1p (1992-Date)	Circular disc	20.3	1.52	0.025	94% Mild steel core, 6% copper coating	200/1 (core/coating)	6×10^6 /5.8×10^7 (Core/coating)
2p (1971-1992)	Circular disc	25.9	1.85	n/a	97% Copper, 2.5% zinc and 0.5% tin	1	4.03×10^7
2p (1992-Date)	Circular disc	25.9	2.03	0.025	4% Mild steel core, 6% copper coating	200/1 (Core/coating)	6×10^6 /5.8×10^7 (core/coating)
5p (1990-2011)	Circular disc	18	1.7	n/a	75% Copper and 25% nickel	1	2.91×10^6
5p (2011-Date)	Circular disc	18	1.7	0.025	94% Mild steel core, 6% nickel coating	200/100 (core/coating)	6×10^6 /1.45×10^7 (core/coating)
10p (1990-2011)	Circular disc	24.5	1.85	n/a	75% Copper and 25% nickel	1	2.91×10^6
10p (2011-Date)	Circular disc	24.5	1.85	0.025	94% Mild steel core, 6% nickel coating	200/100 (Core/coating)	6×10^6 /1.45×10^7 (Core/coating)
20p (1982-Date)	Reuleaux heptagonal disc	21.4	1.7	n/a	84% Copper and 16% nickel	1	5.26×10^6
50p (1997-Date)	Reuleaux heptagonal disc	27.3	1.78	n/a	75% Copper and 25% nickel	1	2.91×10^6
£1 (2017-Date)	Inner circular disc enclosed by an annulus with a dodecagonal boundary	15.2 /23.45 (in/out)	2.8 / 2.8 (in/out)	0.05	Nickel plated brass / 70% copper, 24.5% zinc and 5.5% nickel	1 /100/1.15 (In/coating/out)	1.63×10^7 /1.45×10^7/ 5.26×10^6 (In/coating/out)
£2 (1998-Date)	Inner circular disc enclosed by an annulus	21 /28.4 (In/out)	2.5 /2.5 (In/out)	n/a	75% Copper and 25% nickel/ 97% copper, 2.5% zinc and 0.5% tin	1 /1.15 (In/out)	2.91×10^6 / 1.93×10^7 (In/out)

Table 1: Set of British coins 1p, 2p, 5, 10p, £1, and £2 : Coin shape, dimensions and electrical properties. Grey rows indicate coins whose composition includes a solid magnetic core with a thin coating of a different material. With the exception of old £1 coins (not included), each denomination remains in circulation.

consisting of 6 817, 11 175, 5 583 and 6 735 prisms, respectively. In the case of the coated 1p coin, we show, in Figure 1, a cut through the mesh for the object to illustrate the prisms used to describe the copper coating and the tetrahedra used to describe the mild steel core.

In each case, converged results were obtained for frequencies $1 \times 10^1 \leqslant \omega \leqslant 1 \times 10^8$ rad/s by using
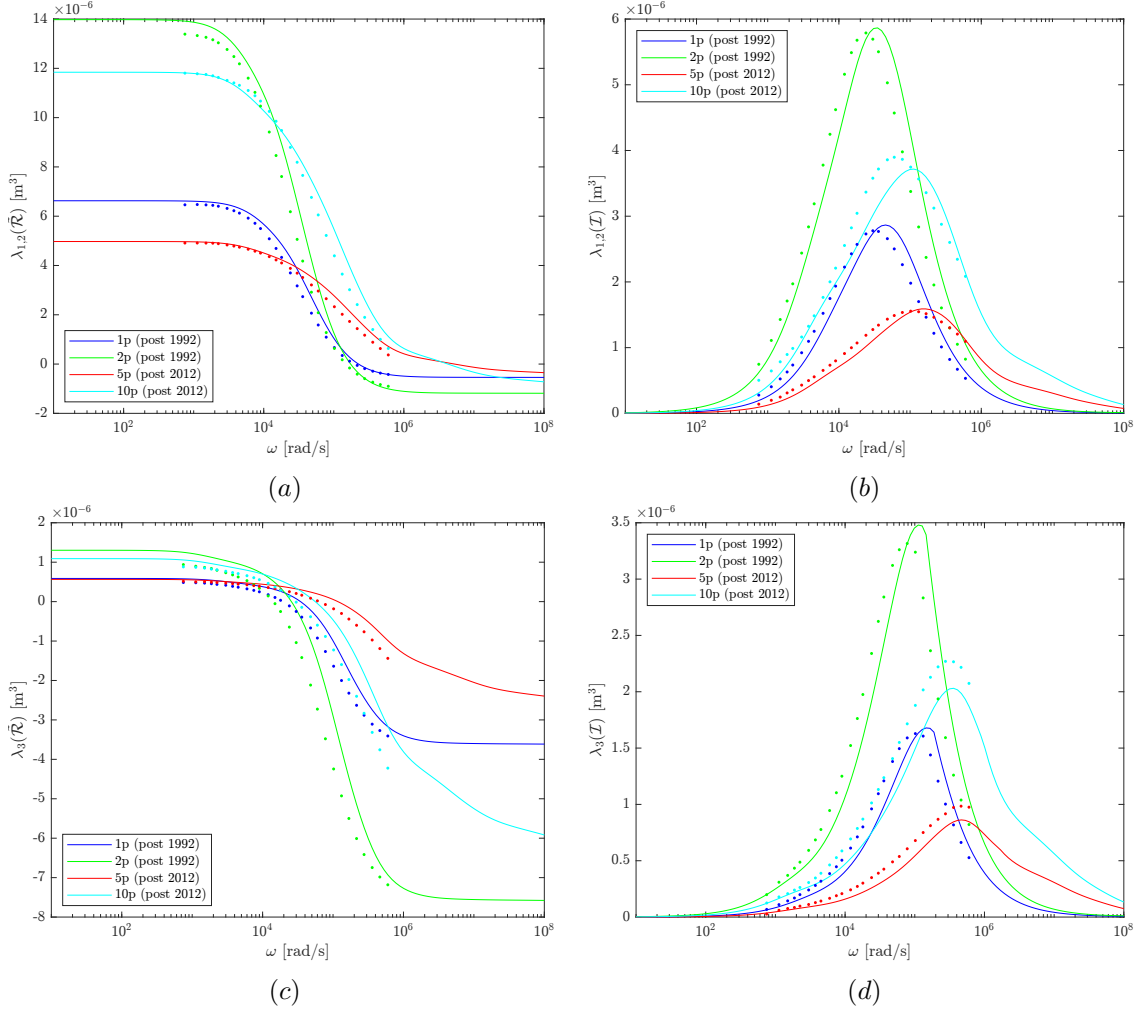
Figure 8: British conducting magnetic 1p (post-1992), 2p (post-1992), 5p (post-2011) and 10p (post 2011) showing the comparison between the measured and computed MPT spectral signature for the coins. The computed MPT spectral signatures use POD with full order model solution snapshots at logarithmically spaced frequencies using uniform $p = 3$ elements on unstructured meshes of $89\,976$, $134\,874$, $82\,004$ and $101\,777$ tetrahedra, respectively, with the addition of a single prismatic layer in each case consisting of $6\,817$, $11\,175$, $5\,583$ and $6\,735$ prisms: (a) $\lambda_{1,2}(\tilde{\mathcal{R}}(\alpha B, \omega, \sigma_*, \mu_r))$, (b) $\lambda_{1,2}(\mathcal{I}(\alpha B, \omega, \sigma_*, \mu_r))$, (c) $\lambda_3(\tilde{\mathcal{R}}(\alpha B, \omega, \sigma_*, \mu_r))$ and (d) $\lambda_3(\mathcal{I}(\alpha B, \omega, \sigma_*, \mu_r))$. In the figure, the measured eigenvalues for each coin are indicated by the appropriately coloured dots.

the POD reduced order model, with $N = 13$ full order solution snapshots computed using order $p = 3$ elements at logarithmically spaced frequencies. Figure 8 shows the computed eigenvalues $\lambda_i(\tilde{\mathcal{R}})$ and $\lambda_i(\mathcal{I})$ as a function of exciting frequency together with the measured MPT spectral signatures obtained using the approach described in Section 4. For the frequencies where measurements are available, we observe good agreement between the computed and measured MPT spectral signatures.

The metallic materials and assumed material parameters employed for the non-magnetic 1p (pre-1992), 2p (pre-1992), 5p (pre-2011), 10p (pre-2011), 20p, 50p, £1, and £2 coins currently in circulation are as stated in Table 1. We observe that, with the exception of the £1 and £2 coins, these have $\mu_r = 1$ and, in the case of these two coins, they were modelled with $\mu_r = 1.15$ in the outer ring to reflect the paramagnetic constitutive behaviour of copper, nickel zinc mixtures (Gross 1951) and the magnetostatic response in the measurements. The discretisations and computational models employed are as stated in Ledger et al. (2021) since the non-magnetic behaviour of these coins means that the skin depth can be adequately captured without the inclusion of a prismatic layer. In the case of the £1 coin, the thin nickel coating is observed, via measurement (Figure 9), to have a negligible impact on the MPT, we therefore simplify our model of the £1 coin to that of a bimetallic disk without the nickel coating. In Figure 9 we show the comparison between the computed and measured MPT spectral signatures in the form of $\lambda_i(\tilde{\mathcal{R}})$ and $\lambda_i(\mathcal{I})$ as a function of exciting frequency for these coins where good agreement is observed with the measurement data.
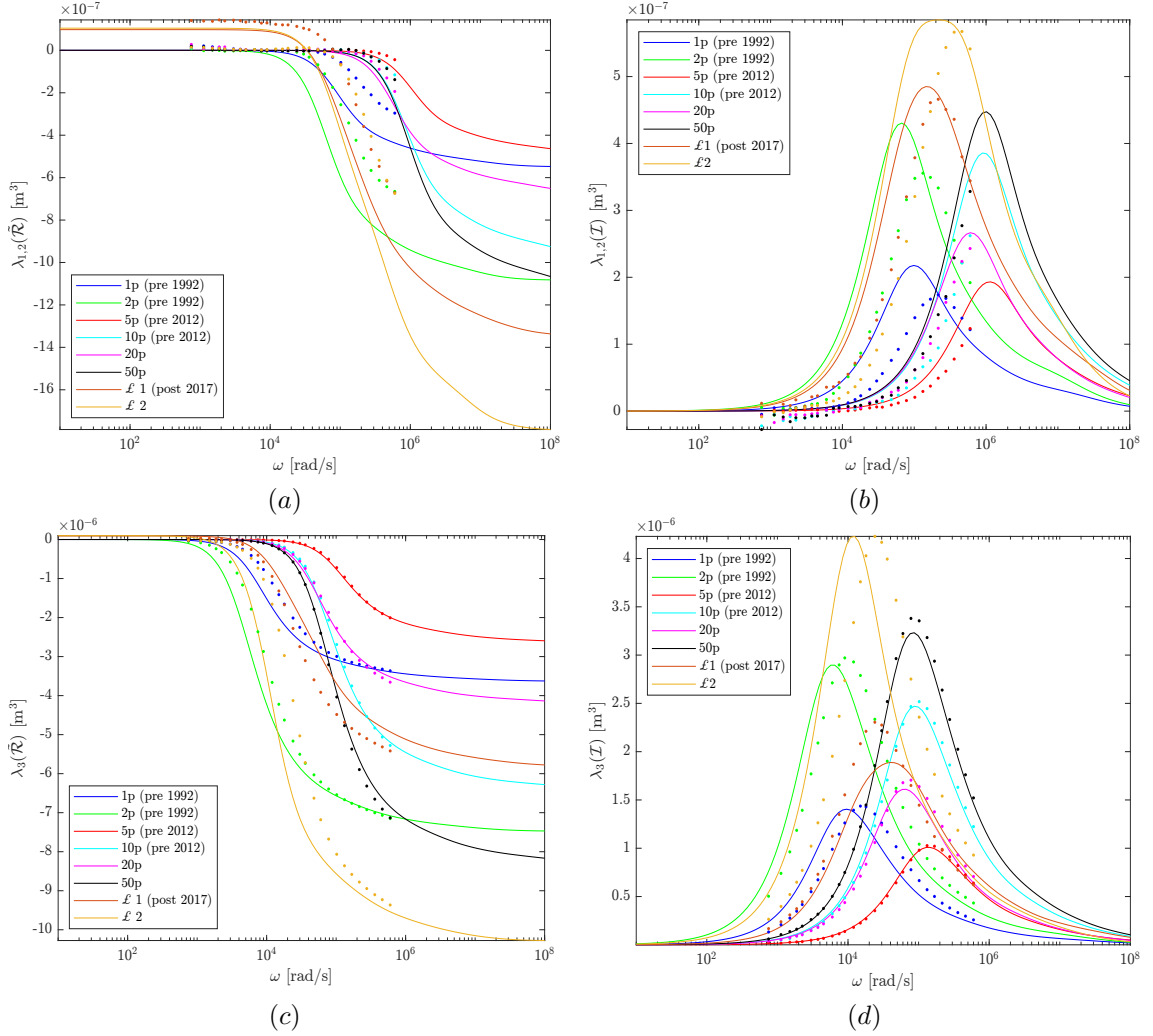
13

Figure 9: British conducting non-magnetic 1p (pre-1992), 2p (pre-1992), 5p (pre-2011), 10p (pre-2011), 20p, 50p, £1 and £2 showing the comparison between the measured and computed MPT spectral signature for the coins (using discretisations similar to those stated in Ledger et al. (2021)): (a) $\lambda_{1,2}(\tilde{\mathcal{R}}(\alpha B, \omega, \sigma_*, \mu_r))$, (b) $\lambda_{1,2}(\mathcal{I}(\alpha B, \omega, \sigma_*, \mu_r))$, (c) $\lambda_3(\tilde{\mathcal{R}}(\alpha B, \omega, \sigma_*, \mu_r))$ and (d) $\lambda_3(\mathcal{I}(\alpha B, \omega, \sigma_*, \mu_r))$. In the figure, the measured eigenvalues for each coin are indicated by the appropriately coloured dots.

5.2.1 Errors and uncertainties in MPT measurements and computations

We recall that accuracy is a measure of the agreement between a measured and accepted value and precision is a measure of consistency and repeatability of an experiment. With regard to measured spectral signatures, the measurement apparatus keeps uncertainties and unavoidable errors that affect the accuracy and precision to a minimum. For example, the use of the TOM, together with the geometry of the coins, mean that these objects are firmly secured in position during measurement. However, there is the potential for background interference from the metallic structure of the building. To minimise this, and improve their accuracy, measurements were taken in a room isolated as much as possible from the building structure and repeated measurements were taken in isolation to avoid background contamination. Lower metal content objects produce a weaker signal, that is harder to measure, compared to the stronger signal produced by higher metal content objects. Nevertheless, the apparatus was designed for the measurement of minimum metal content anti-personnel landmines, which have a lower metal content than the lowest denomination 1p, 2p coins considered (Özdeğer, Ledger & Peyton 2022). From previous work Özdeğer et al. (2021), for objects secured in position, the apparatus has been shown to accurately measure MPT coefficients of the order of 10^{-7} m^3, if not smaller. However, the post-processing of the data means that reliable measurements can be made to around 10% of the magnitude of the peak MPT values and, hence, the larger magnitude MPT coefficients are expected to be captured more accurately than the smaller ones. Furthermore, as described in Section 4, all measurements are subject to thermal drift of the measurement

system, which will affect their precision.

Our computational models are also subject to uncertainties and errors. When modelling the coins, we do not have exact values of the true conductivities and permeabilities of the metallic materials used in the coin and our geometric models are based on approximations to the true geometry of the coin. Each individual coin can have variations in both its size and composition, depending on when it was minted and how long it has been in circulation. Our computational results are also subject to modelling errors associated with our finite element discretisation, approximations made in our POD reduced order model, and approximate linear solution techniques and post-processing. We minimise these by ensuring that our computational solutions are converged and using suitable tolerances, and so are confident that our solutions have at least the same accuracy as the measurements for given set of material parameters and object geometry.

To understand the precision of the measured MPT signatures, 10 repeat measurements of a single 1p (post 1992) coin and a single £1 (post 2017) coin were taken. For each frequency, and each coin measurement, we construct 95% confidence intervals for the mean values of $\lambda_i(\tilde{\mathcal{R}})$ and $\lambda_i(\mathcal{I})$ obtained from the measurements, which are shown together with the mean values in Figure 10 in the form of markers with error bars. The measured MPT signature for the 1p and £1 coins exhibits a high degree of precision at all frequencies, as indicated by the small confidence intervals, with a small increase in the size of the confidence interval towards the smallest frequencies. Note that, if repeat measurements of different 1p and £1 coins were taken, we would expect their confidence intervals to become larger due to variations in the object size and compositions of coins minted on different dates and by different machines.

Also included in Figure 10 are curves indicating the spread in the converged computed MPT spectral signatures where, in addition to the geometric and material properties stated in Table 1, we take account of uncertainties in the object size and material parameters. The spread in the data is illustrated by the construction of 5th and 95th percentiles and median values for the simulated $\lambda_i(\tilde{\mathcal{R}})$ and $\lambda_i(\mathcal{I})$ for these different object sizes and materials[2]. In the case of the 1p and £1 coins, the data is generated by drawing samples $\alpha \sim N(\alpha_m, \alpha_s)$, where $N(\alpha_m, \alpha_s)$ refers to a normal distribution with mean α_m and standard deviation α_s, and take $\alpha_m = 1 \times 10^{-3}$ m and $\alpha_s = 5 \times 10^{-5}$ m, which have been constructed based on comparing the dimensions of a sample of coins. To take account of possible variations in the conductivity, we draw samples $\sigma_* \sim N((\sigma_*)_m, (\sigma_*)_s)$, with mean $(\sigma_*)_m$ and standard deviation $(\sigma_*)_s$. For the 1p coin, $(\sigma_*)_m = 2.95 \times 10^7$ S/m, corresponds to the mean conductivity of the steel core and copper cladding described in Table 1, and $(\sigma_*)_s = 0.03(\sigma_*)_m$ (Ho et al. 1983). Similarly, for the £1 coin, we take $(\sigma_*)_m = 1.078 \times 10^7$ S/m for the mean of the conductivities in the inner and outer parts of the coin and $(\sigma_*)_s = 0.03(\sigma_*)_m$ (Ho et al. 1983) and use these samples to scale the conductivities of each part of the coin by the same factor. New MPT spectral signatures for each α, σ_* combination were obtained at negligible computational cost using the scaling results derived in Wilson & Ledger (2021). We observe that the mean value of the measured $\lambda_i(\tilde{\mathcal{R}})$ and $\lambda_i(\mathcal{I})$ lies within (or very close to) the corresponding 5th and 95th percentiles curves for our simulations giving us a high degree of confidence in our both our experimental and computational results, despite the uncertainties outlined above. If desired, these percentiles could be improved by also taking in to account possible variations in μ_r, which we incorporate for the cases of magnetic keys in the following.

5.3 Common household keys

We consider a range of different household keys (notably Keys 4, 6, 9 and 11, which reflect a sample of a larger set of different key types), photographs of which are provided in Figure 11. The approximate dimensions of the keys and their possible compositions are listed in Table 2. For the sample keys their exact material composition is unknown and the values in the table has been informed on the basis of common material parameters of metals used in keys, the key's colour and whether the key is magnetic or not. Typical metals for keys include brass, steel, nickel silver, and sometimes nickel, aluminium or zinc and, depending on the particular alloy, there can be some variation in both its relative permeability and conductivity. For example, from Ho et al. (1983), a common form of brass is a 70%-30% copper-zinc alloy, which at 20°C has a conductivity of $1.64 \times 10^7 \pm 3\%$ S/m. We have chosen to model brass as $\sigma_* = 1.5 \times 10^7$ S/m to follow Ledger et al. (2021) and *Conductivity Of Metals Sorted By Resistivity* (n.d.), which is towards the lower limit.

---

[2]The use of confidence intervals for the computed $\lambda_i(\tilde{\mathcal{R}})$ and $\lambda_i(\mathcal{I})$ is not appropriate as each computational experiment considers a different material and a different geometry and hence each MPT signature characterisation is for a different object rather than repeated simulations of the same object using different discretisations
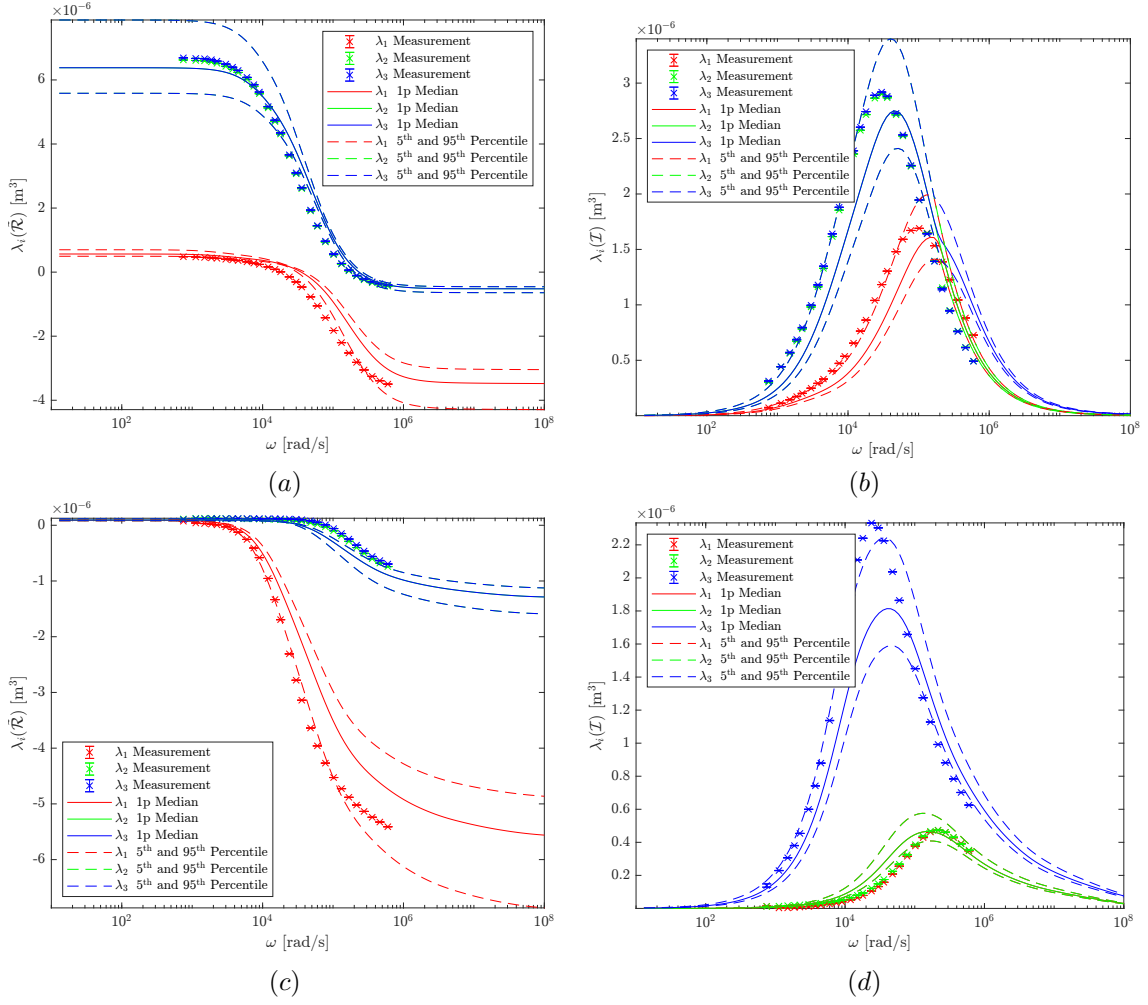
Figure 10: British conducting magnetic 1p and non-magnetic £1 coins showing a comparison between measured and computed eigenvalues for the MPT spectral signatures including the mean and 95% confidence intervals for the measured eigenvalues and the 5th and 95th percentiles on the simulated eigenvalues: (a) $\lambda_i(\tilde{\mathcal{R}}(\alpha B, \omega, \sigma_*, \mu_r))$, (b) $\lambda_i(\m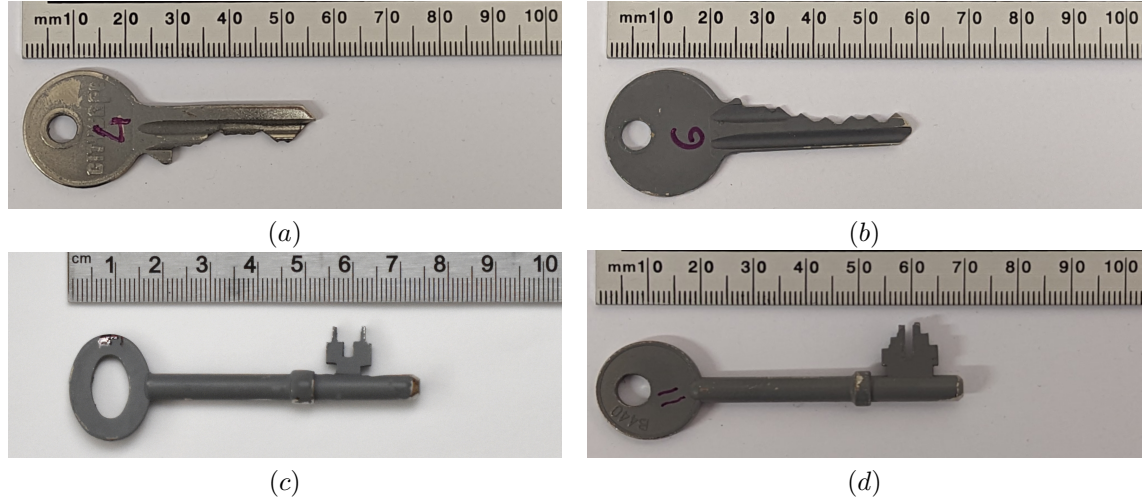athcal{I}(\alpha B, \omega, \sigma_*, \mu_r))$ for the 1p coin and (c) $\lambda_i(\tilde{\mathcal{R}}(\alpha B, \omega, \sigma_*, \mu_r))$, (d) $\lambda_i(\mathcal{I}(\alpha B, \omega, \sigma_*, \mu_r))$ for the £1 coin.

Figure 11: Photographs of a sample of British keys, which have been painted grey to aid with the imaging process: (a) Key 4, (b) Key 6, (c) Key 9 and (d) Key 11.

Key	Colour	Total length [10^{-3} m]	Total width [10^{-3} m]	Thickness [10^{-3} m]	Composition	Relative Permeability (μ_r)	Conductivity (σ_*) [S/m]
Key 4	Silver	56	24	2	Mild steel	100-300	$10^6 - 10^7$
Key 6	Bronze	70	24	2	Brass	1	1.5×10^7 (26% IACS) (*Conductivity Of Metals Sorted By Resistivity* n.d.)
Key 6	Silver	70	24	2	Nickel plated brass (5×10^{-5} m plating (Whittington & Rose 2014))	1/ 100 (Core/coating)	$1.5 \times 10^7/1.46 \times 10^7$ (*Conductivity Of Metals Sorted By Resistivity* n.d.)
Key 6	Silver	70	24	2	Nickel silver	1.0 - 1.1	1.276×10^7 (22% IACS)(Westman et al. 1972)
Key 9	Silver	78	24	7	Mild steel	100-300	$10^6 - 10^7$
Key 11	Bronze	70	25	7	Brass	1	1.5×10^7 (26% IACS)

Table 2: Typical house keys: Sizes, colour and composition of some typical house keys. The rows indicated in grey are magnetic.

5.3.1 Key 4

Key 4 is a magnetic corrugated key, which is typically used in pin-tumbler locks. The procedure described in Section 3.2 is applied to generate a 170 820 vertex point cloud to describe the non–dimensional object B with dimensions such that $\alpha = 1 \times 10^{-3}$ m, which was then downsampled to a quasi-uniform 3120 vertex point cloud, with average edge length 0.784 units, and converted into a faceted .step format. To generate a MPT-Calculator compatible mesh, we insert the object B into a $[-1000, 1000]^3$ units non-conducting region, resulting in mesh with 27 478 unstructured tetrahedra. The maximum surface element size for the key is limited by the density of the point cloud, thus the element size on the surface of the key will have an average length of 0.784 units, however the element size away from the surface of B, such as the non-conducting region, are not limited by the point cloud, instead we limit the element size by $\max h = 1000$ units and $\min h = 5$ units. Figure 12 provides an example of each stage of the imaging process outlined in Section 3.2 including the resulting surface discretisation for the object B in Figure 12 (d).

Key 4 is known to be magnetic, thus we model the key as mild steel, which corresponds to a cheap common key material. For steel, the conductivity is well defined as $1 \times 10^6 \leqslant \sigma_* \leqslant 1 \times 10^7$ S/m, however the relative permeability can vary substantially by several orders of magnitude. For this reason, we consider

a range of μ_r drawn from a normal distribution $\mu_r \sim N((\mu_r)_m, (\mu_r)_s)$ with $(\mu_r)_m = 200$ and $(\mu_r)_s = 50$ and note that high values of μ_r are not expected to result in significant change in the MPT spectral signature (Elgy & Ledger 2023b). To ensure that accurate results are obtained, we introduce two thin layers of prismatic elements of thickness δ/α and $2\delta/\alpha$ units resulting in a mesh with 12 479 prisms and 27 478 unstructured tetrahedra.
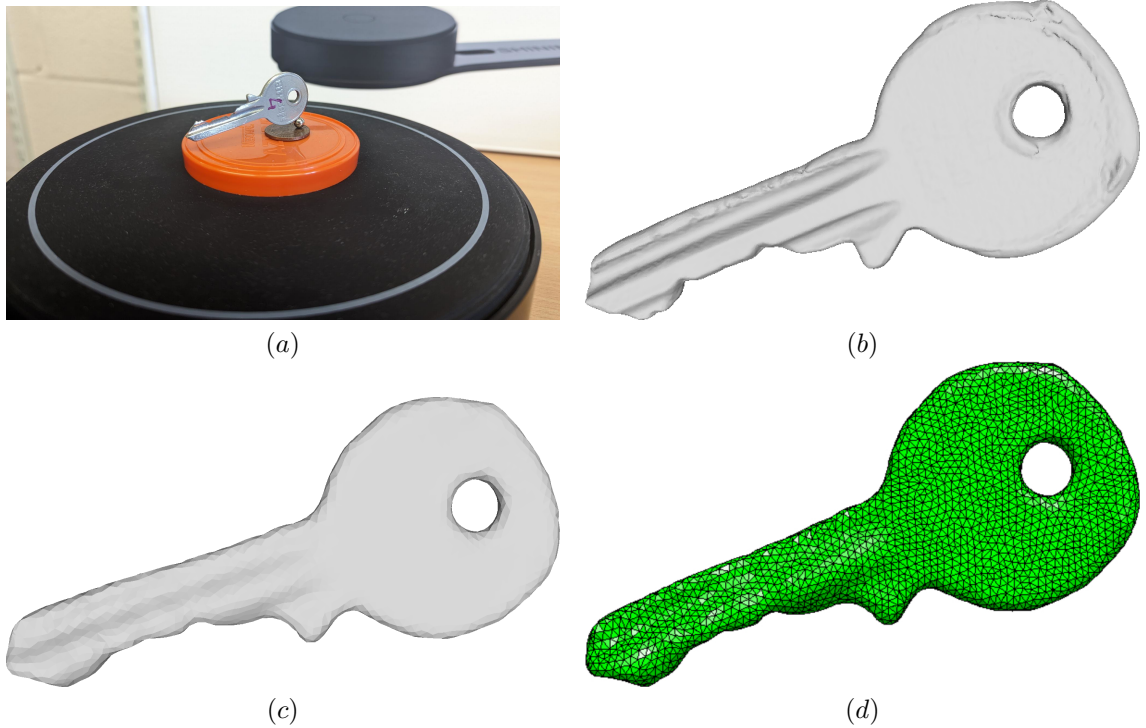

Figure 12: Illustration of the imaging procedure detailed in Section 3.2 applied to Key 4 showing: (a) object on the scanner, (b) fine surface description associated with high density point cloud, (c) coarser surface description corresponding to downsampled quasi-uniform point cloud and (d) the associated coarser surface triangulation, which is then imported into `Netgen` to create a volumetric mesh of unstructured tetrahedra to describe B and the surrounding region to the truncation boundary.

To understand the variation in the MPT signatures for different material parameters and objects sizes for Key 4, Figure 13 shows the median and 5$^{\text{th}}$ and 95$^{\text{th}}$ percentiles for $\lambda_i(\tilde{\mathcal{R}}(\alpha B, \omega, \sigma_*, \mu_r))$ and $\lambda_i(\mathcal{I}(\alpha B, \omega, \sigma_*, \mu_r))$. This was obtained, by generating 10 samples of μ_r drawn from $\mu_r \sim N((\mu_r)_m, (\mu_r)_s)$, with $(\mu_r)_m = 200$ and $(\mu_r)_s = 50$, 10 object sizes as $\alpha \sim N(\alpha_m, \alpha_s)$, with $\alpha_m = 1 \times 10^{-3}$ m and $\alpha_s = 0.02\alpha_m$, and 10 conductivities drawn from $\sigma_* \sim N((\sigma_*)_m, (\sigma_*)_s)$, with $(\sigma_*)_m = 6 \times 10^6$ S/m and $(\sigma_*)_s = 2.5 \times 10^6$ S/m. The choice of α_s is based on an generous estimate of the discrepancy between the size of the original object (Figure 12 (a)) and the final coarse mesh (Figure 12 (c)), taking into account the point cloud density of the scanner (2×10^{-4} m) and defects in the mesh resulting from the scanning process. Since we do not have a ground truth geometry description for this object, the discrepancy between the true geometry and the point cloud description is based on visual inspection. The choice of $(\sigma_*)_m$, and $(\sigma_*)_s$ correspond to the same steel material used in Section 5.2. The computed MPT spectral signatures for different μ_r were obtained via repeat simulation using POD with 13 full order model solutions at logarithmically spaced snapshot frequencies with uniform order $p = 4$ elements and the anisotropic mesh described above, while, for the other parameters, the scaling results in Wilson & Ledger (2021) were employed. The figure shows that the single set of measurements taken do generally lie within (or close to) the 5$^{\text{th}}$ and 95$^{\text{th}}$ percentiles for the simulations. However, compared, to the coins, there is an increased potential for the key to move slightly during the measurements and also we have less confidence over the true material parameters of the metals used in the key and the modelled geometry, which explain the results shown.

5.3.2 Key 6

Key 6 is a corrugated key and is weakly magnetic or non-magnetic. The procedure described in Section 3.2 is applied to generate a 119 606 vertex point cloud to describe the non–dimensional object B with dimensions such that $\alpha = 1 \times 10^{-3}$ m, which was then downsampled to a quasi-uniform 5614 vertex point cloud, with
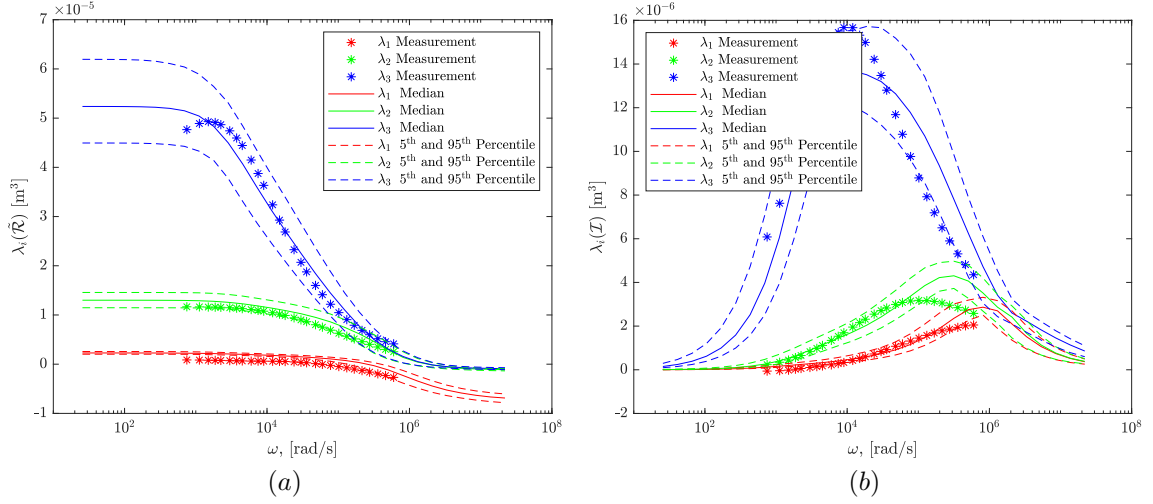
Figure 13: Key 4 MPT spectral signatures showing the variation in the computational results if the material is mild steel with $\alpha \sim N(\alpha_m, \alpha_s)$, $\sigma_* \sim N((\sigma_*)_m, (\sigma_*)_s)$, $\mu_r \sim N((\mu_r)_m, (\mu_r)_s)$ compared with measurement data. The computed MPT spectral signatures use POD with full order model solution snapshots at logarithmically spaced frequencies using uniform $p = 4$ elements on a mesh of 7 311 prisms and 32 918 unstructured tetrahedra: (a) $\lambda_i(\tilde{\mathcal{R}}(\alpha B, \omega, \sigma_*, \mu_r))$, (b) $\lambda_i(\mathcal{I}(\alpha B, \omega, \sigma_*, \mu_r))$, for $i = 1, 2, 3$.

average edge length 0.642 units, and converted into a faceted `.step` format. As with Key 4, we insert the object B into a $[-1000, 1000]^3$ units non-conducting region, resulting in a mesh with 41 834 unstructured tetrahedra. The maximum surface element size for the key is limited by the density of the point cloud, thus the element size on the surface of the key will have an average length of 0.642 units. In the same way as Key 4, we limit the element size away from the surface of the object by specifying max $h = 1000$ units, min $h = 5$ units. The resulting surface discretisation for the object B is shown in Figure 14.
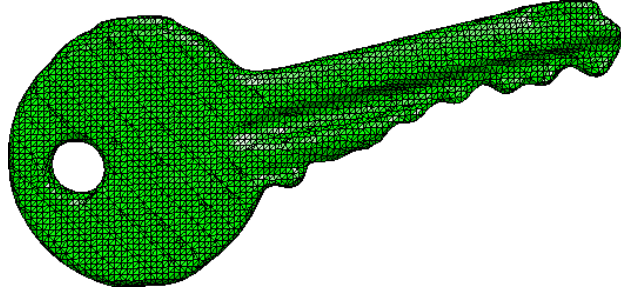

Figure 14: Key 6: Surface mesh description. The complete volume mesh contains 11 227 prisms and 41 834 unstructured tetrahedra in total.

Using the aforementioned tetrahedral mesh, we consider the MPT characterisations assuming the object composition is brass, nickel-plated brass, and nickel-silver, in turn, using the material parameters stated in Table 2. In the case of nickel-plated brass, a 5×10^{-5} m thick nickel coating is assumed (upper estimate for the thickness of the coating (Westman et al. 1972)), which is modelled by using a single boundary layer with 11 227 prisms in a mesh with an unchanged number of tetrahedra. In each case, uniform order $p = 3$ elements were found to produce converged results at the $N = 13$ frequency snapshots and the complete MPT spectral signature for $1 \times 10^1 \leqslant \omega \leqslant 1 \times 10^8$ rad/s was obtained using the PODP method with a truncation tolerance of 10^{-6}. We show in Figure 15 comparisons of the MPT spectral signatures for $\lambda_1(\tilde{\mathcal{R}})$ and $\lambda_3(\mathcal{I})$, which are largest in magnitude. In this figure, we observe that modelling the key as nickel-silver produces the closest match to the measurements, which notably is able to capture the small magnetostatic response that is not possible using a brass or nickel-plated brass model.

As with Key 4, we consider the uncertainties in the object size and its material parameters for Key 6. While the imaging process is quoted as being accurate to $\pm 2 \times 10^{-4}$ m, further inaccuracies are also introduced when the point cloud is downsampled and the unstructured mesh of tetrahedra is generated. There are also additional uncertainties regarding the key's relative permeability and conductivity. To estimate percentiles for the MPT spectral signatures for the key, we introduce permutations of the MPT spectral signature corresponding to variations in μ_r, σ_*, and α in a similar manner to as described in
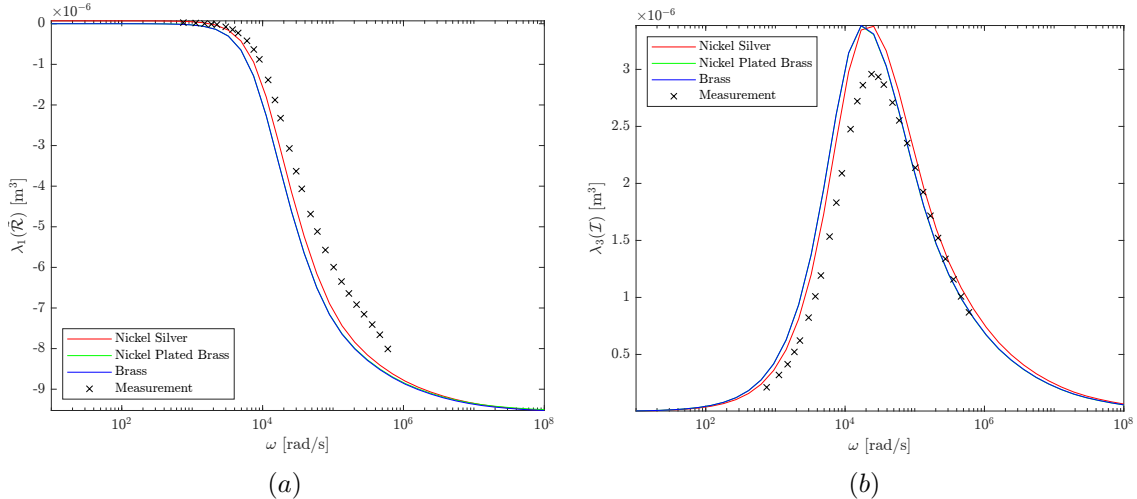
19

Figure 15: Key 6 MPT spectral signatures showing the computed spectral signature assuming the object composition is brass, nickel-plated brass and nickel-silver compared with the experimental measurements. The computed MPT spectral signatures use POD with full order model solution snapshots at logarithmically spaced frequencies using uniform $p = 3$ elements on a mesh of $41\,834$ unstructured tetrahedra (with $11\,227$ additional prisms to model the nickel plating): (a) $\lambda_1(\mathcal{R}(\alpha B, \omega, \sigma_*, \mu_r))$, (b) $\lambda_3(\mathcal{I}(\alpha B, \omega, \sigma_*, \mu_r))$.

Section 5.2.1. In particular, we generate 10 different MPT spectral signatures corresponding to object sizes drawn as $\alpha \sim N(\alpha_m, \alpha_s)$, with $\alpha_m = 1 \times 10^{-3}$ m and $\alpha_s = 0.02\alpha_m$. Similarly, we generate 10 MPT spectral signatures corresponding to conductivities drawn from $\sigma_* \sim N((\sigma_*)_m, (\sigma_*)_s)$, where $(\sigma_*)_m = 1.276 \times 10^7$ S/m was obtained from quoted conductivities for nickel silver (Westman et al. 1972) and $(\sigma_*)_s$ is taken to be $0.03 (\sigma_*)_m$ corresponding to the uncertainty for copper based alloys stated in Ho et al. (1983). For μ_r, we generate 10 samples drawn from $\mu_r \sim N((\mu_r)_m, (\mu_r)_s)$ with $(\mu_r)_m = 1.05$ and $(\mu_r)_s = 0.025$, so that the majority of samples lie within the expected bounds $1 \leqslant \mu_r \leqslant 1.1$ obtained from observations of the variation in the MPT spectral signature. This data set is used to construct the median, 5$^{\text{th}}$, and 95$^{\text{th}}$ percentiles for the MPT spectral signatures shown in Figure 16. In a similar manner to Key 4, the figure shows that the single set of measurements taken do generally lie within (or close to) the 5$^{\text{th}}$ and 95$^{\text{th}}$ percentiles for the simulations. We again note there is an increased potential for the key to move slightly during the measurements and also we have less confidence over the true material parameters of the metals used in the key and the modelled geometry, which explain the results shown.

5.3.3 Key 9

Key 9 is a magnetic mortice key. The procedure described in Section 3.2 is applied to generate a $114\,899$ vertex point cloud to describe the non–dimensional object B with dimensions such that $\alpha = 1 \times 10^{-3}$ m, which was then downsampled to a quasi-uniform $3\,290$ vertex point cloud and converted into a faceted `.step` format. To generate a `MPT-Calculator` compatible mesh, we insert the non–dimensional object B into a $[-1000, 1000]^3$ units non-conducting region. By also including a thin ($h = 5 \times 10^{-3}$ units) layer of prismatic elements, this resulted in a mesh with $6\,613$ prisms and $67\,512$ unstructured tetrahedra. The resulting surface mesh is illustrated in Figure 17. This is similar to Key 6 and results in a mean surface element size of the object of 0.870 units.

We conjecture that the key is made of steel, as a common magnetic key material. As with the previous keys, we consider the effect of uncertainty in the object size and material parameters by constructing samples corresponding to $\alpha \sim N(\alpha_m, \alpha_s)$, with $\alpha_m = 1 \times 10^{-3}$ m and $\alpha_s = 0.02\alpha_m$, using the same conductivity distribution $\sigma_* \sim N((\sigma_*)_m, (\sigma_*)_s)$ and relative permeability distribution $\mu_r \sim N((\mu_r)_m, (\mu_r)_s)$ as Key 4 shown in Section 5.3.1. MPT spectral signatures corresponding to different μ_r were generated using uniform order $p = 4$ elements at the $N = 13$ frequency snapshots snapshots and the complete MPT spectral signature for $1 \times 10^1 \leqslant \omega \leqslant 1 \times 10^8$ rad/s was obtained using the PODP method with a truncation tolerance of 10^{-6}. Then, to estimate percentiles for the MPT spectral signatures for the key, we introduce permutations of the MPT spectral signature corresponding to variations in μ_r, σ_*, and α in a similar manner to as described in Section 5.2.1.

Figure 18 shows the resulting median, 5$^{\text{th}}$, and 95$^{\text{th}}$ percentiles for the MPT spectral signatures along with the measured data for $\lambda_i(\widetilde{\mathcal{R}}(\alpha B, \omega, \sigma_*, \mu_r))$ and $\lambda_i(\mathcal{I}(\alpha B, \omega, \sigma_*, \mu_r))$. Similar to the previous keys,
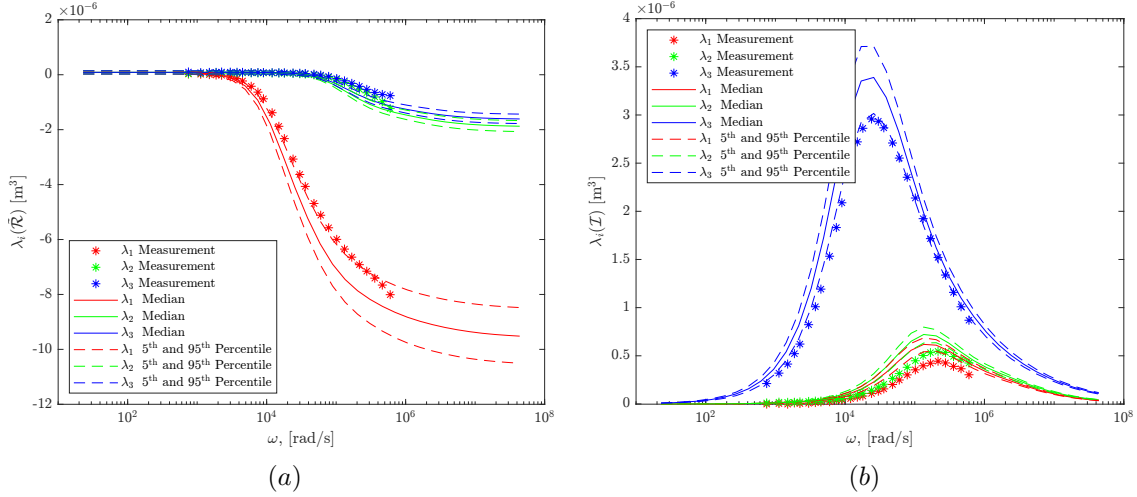
$$(a) \qquad\qquad (b)$$

Figure 16: Key 6 MPT spectral signatures showing the variation in the computational results if the material is nickel-silver with $\alpha \sim N(\alpha_m, \alpha_s)$, $\sigma_* \sim N((\sigma_*)_m, (\sigma_*)_s)$, $\mu_r \sim N((\mu_r)_m, (\mu_r)_s)$ compared with measurement data. The computed MPT spectral signatures use POD with full order model solution snapshots at logarithmically spaced frequencies using uniform $p = 3$ elements on a mesh 41 834 of unstructured tetrahedra: (a) $\lambda_i(\tilde{\mathcal{R}}(\alpha B, \omega, \sigma_*, \mu_r))$, and (b) $\lambda_i(\mathcal{I}(\alpha B, \omega, \sigma_*, \mu_r))$ for $i = 1, 2, 3$.
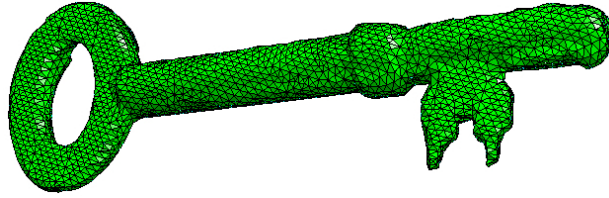

Figure 17: Key 9: Surface mesh description. The complete volume mesh contains 6 613 prisms and 67 512 unstructured tetrahedra in total.

the figure shows that the single set of measurements taken do generally lie within (or close to) the 5th and 95th percentiles for the simulations with the differences attributed to the uncertainty of the geometry and metallic materials used in the key and possible movement of the key as before.

5.3.4 Key 11

Key 11 is a non-magnetic mortice key. As with the other keys, Key 11 was first scuffed using sandpaper before being spray-painted matt grey. During this time it was noticed that the key consists of a thin chrome coating over bronze coloured metal, which together with its magnetostatic response indicated that it is likely to be made of brass. The procedure described in Section 3.2 is again applied to generate a 137 230 vertex point cloud to describe the non–dimensional object B with dimensions such that $\alpha = 1 \times 10^{-3}$ m, which was thendownsampled to a quasi-uniform 4 425 vertex point cloud, with average edge length 0.725 units, and converted into a faceted .step format. In the same way as the other keys, we insert the non–dimensional object B into a $[-1000, 1000]^3$ units non-conducting region, resulting in a mesh with 37 084 unstructured tetrahedra. The maximum surface element size for the key is limited by the density of the point cloud, thus the element size on the surface of the key will have an average length of 0.724 units. As with the other keys, we limit the size of the elements away from the surface of B by specifying $\max h = 1000$ units, $\min h = 5$ units. The resulting surface mesh is illustrated in Figure 19.

Using the aforementioned tetrahedral mesh, we consider the MPT characterisations assuming the object composition is brass using the material parameters stated in Table 2. Uniform order $p = 4$ elements were found to produce converged results at the $N = 13$ frequency snapshots and the complete MPT spectral signature for $10 \leqslant \omega \leqslant 10^8$ rad/s was obtained using the PODP method with a truncation tolerance of 10^{-6}. In this case, we have a high degree of certainty in the material parameters and so only consider the impact of the uncertainty in the geometrical modelling. In this case, considering the discrepancies between the mesh and physical object, shown in Figure 19, we estimate that $\alpha_s = 0.02\alpha_m$. Then, to estimate percentiles for the MPT spectral signatures for the key, we introduce permutations of the MPT spectral signature corresponding to variations in α (only) in a similar manner to as described in Section 5.2.1.
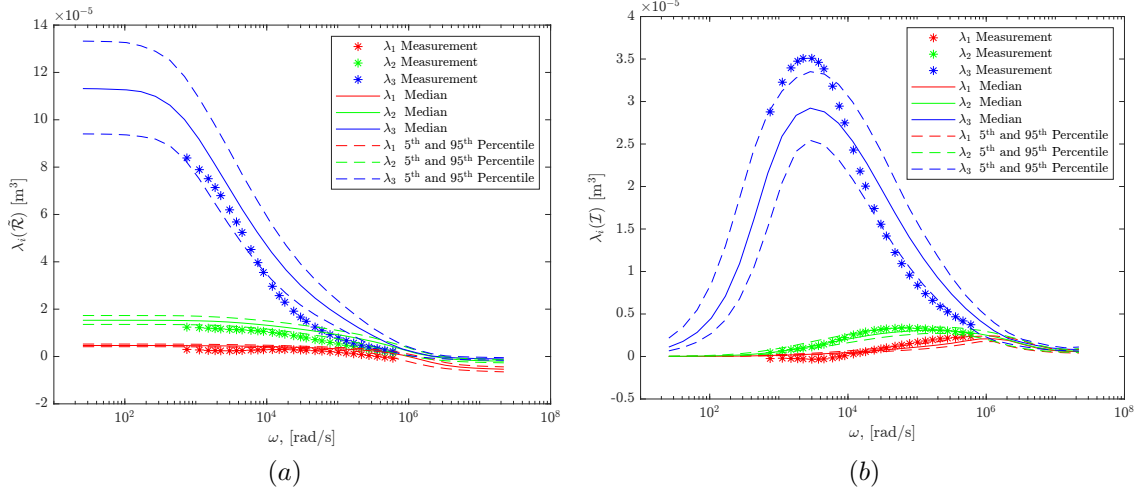
Figure 18: Key 9 MPT spectral signatures showing the variation in the computational results if the material is steel with $\alpha \sim N(\alpha_m, \alpha_s)$, $\sigma_* \sim N((\sigma_*)_m, (\sigma_*)_s)$, $\mu_r \sim N((\mu_r)_m, (\mu_r)_s)$ compared with measurement data. The computed MPT spectral signatures use POD with full order model solution snapshots at logarithmically spaced frequencies using uniform $p = 4$ elements on a mesh of $41\,834$ unstructured tetrahedra: (a) $\lambda_i(\tilde{\mathcal{R}}(\alpha B, \omega, \sigma_*, \mu_r))$, and (b) $\lambda_i(\mathcal{I}(\alpha B, \omega, \sigma_*, \mu_r))$ for $i = 1, 2, 3$.
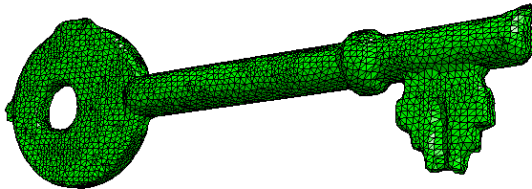

Figure 19: Key 11: Surface mesh description. The mesh contains $37\,084$ unstructured tetrahedra in total.

Figure 20 shows the resulting median, 5th, and 95th percentiles for the MPT spectral signatures along with the measured data for $\lambda_i(\tilde{\mathcal{R}}(\alpha B, \omega, \sigma_*, \mu_r))$ and $\lambda_i(\mathcal{I}(\alpha B, \omega, \sigma_*, \mu_r))$ for this key. We observe that the measurement data is in close agreement with the median curves for $\lambda_i(\tilde{\mathcal{R}})$ and $\lambda_i(\mathcal{I})$ and falls within the 5th and 95th percentiles for all frequencies.

6 Conclusion

This paper has presented computations and measurements of MPT characterisations of highly conducting magnetic objects, which exhibit a high μ_r. Additionally, we consider characterisations of objects that are made of layers of different highly conducting magnetic materials. The examples presented include current and past denominations of British coins (which include recent 1p, 2p, 5p and 10p coins that have a layered construction with a steel core) and examples of different keys (including those made of steel and nickel silver). To accurately resolve the thin skin depths associated with high μ_r and higher frequencies, we have employed the `NGSolve` finite element library and employed a combination of p–refinement of the finite element basis functions and hybrid meshes of tetrahedral elements combined with thin layers of prismatic elements. These have resulted in accurate computations of MPT object characterisations that are in close agreement with the physical measurements. As the exact material properties of many physical objects are unknown, and there can be variability in the physical object geometries for objects within the same class, we have explored the uncertainty in the computed MPT characterisations for uncertain material parameters and uncertain geometries.

We have also presented a procedure for obtaining geometric models of complex geometries based on imaging when the exact geometry is unknown. We have applied this method to compute MPT characterisations of magnetic and non-magnetic conducting keys and compared our computations with measurements. Additionally, we have again considered the uncertainty in our MPT characterisations given that our ob-
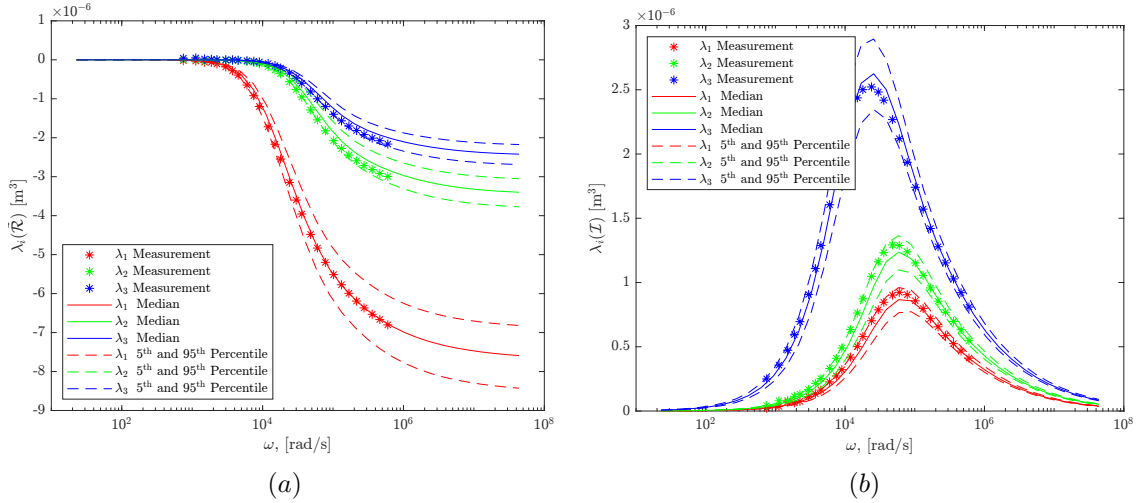
Figure 20: Key 11 MPT spectral signatures showing the variation in the computational results if the material is brass with $\alpha \sim N(\alpha_m, \alpha_s)$, $\sigma_* \sim N((\sigma_*)_m, (\sigma_*)_s)$, $\mu_r = 1$ compared with measurement data. The computed MPT spectral signatures use POD with full order model solution snapshots at logarithmically spaced frequencies using uniform $p = 4$ elements on a mesh of $37\,084$ unstructured tetrahedra: (a) $\lambda_i(\tilde{\mathcal{R}}(\alpha B, \omega, \sigma_*, \mu_r))$, and (b) $\lambda_i(\mathcal{I}(\alpha B, \omega, \sigma_*, \mu_r))$ for $i = 1, 2, 3$.

tained geometric description is subject to modelling errors and the exact material conductivity and relative permeability are unknown. The measured data for these objects lies within the 5th and 95th percentiles describing the spread of the MPT coefficients.

We expect the procedures presented in this work to be invaluable for obtaining MPT characterisations of threat and non-threat objects made of metallic materials with high μ_r. We also expect the ability to take uncertainty in to account to be extremely beneficial when obtaining improved dictionaries of object characterisations for training machine learning classifiers for distinguishing between threat and non-threat objects in metal detection.

In future work, we would also like to take account of the dispersion effects of some magnetic materials on the characterisation of objects by MPTs, such materials exhibit a non-constant μ_r with ω that decreases towards unity for large ω, and also to consider MPT characterisations of objects with anisotropic magnetic materials.

Acknowledgements

References

Abdel-Rehim, O. A., Davidson, J. L., Marsh, L. A., O'Toole, M. D. & Peyton, A. J. (2016), 'Magnetic polarizability tensor spectroscopy for low metal anti-personnel mine surrogates', *IEEE Sensors Journal* **16**, 3775–3783.

Ammari, H., Buffa, A. & Nédélec, J.-C. (2000), 'A justification of eddy currents model for the Maxwell equations', *SIAM Journal on Applied Mathematics* **60**(5), 1805–1823.

Ammari, H., Chen, J., Chen, Z., Garnier, J. & Volkov, D. (2014), 'Target detection and characterization from electromagnetic induction data', *Journal de Mathématiques Pures et Appliquées* **101(1)**, 54–75.

Autodesk (n.d.), 'Fusion 360 — 3d cam, cad, cae & pcb cloud-based software — autodesk', `https://www.autodesk.co.uk/products/fusion-360/overview`. Accessed: 13/10/2022.

Balanis, C. A. (2012), *Advanced Engineering Electromagnetics*, CourseSmart Series, 2nd edn, Wiley, Hoboken, NJ, USA.
URL: *https://books.google.co.uk/books?id=cRkTuQAACAAJ*

Brunning, A. (2014), 'The metals in UK coins', `https://www.compoundchem.com/2014/03/27/the-metals-in-uk-coins/`. Accessed: 08/10/2022.

Conductivity Of Metals Sorted By Resistivity (n.d.), `https://www.effectrode.com/knowledge-base/conductivity-of-metals-sorted-by-resistivity/`. Accessed: 17/07/2023.

Davidson, J. L., Özdeğer, T., Conniffe, D., Murray-Flutter, M. & Peyton, A. J. (2023), 'Classification of threat and nonthreat objects using the magnetic polarizability tensor and a large-scale multicoil array', *IEEE Sensors Journal* **23**(2), 1541–1550.

EinScan (n.d.), 'Download einscan software and latest updates', `https://www.einscan.com/support/download/`. Accessed: 13/10/2022.

Elgy, J. & Ledger, P. D. (2023*a*), 'Improved efficiency and accuracy of the magnetic polarizability tensor spectral signature object characterisation for metal detection'. doi: 10.48550/arXiv.2307.05590, Submitted.

Elgy, J. & Ledger, P. D. (2023*b*), 'Reduced order model approaches for predicting the magnetic polarizability tensor for multiple parameters of interest', *Engineering with Computers* . doi: 10.1007/s00366-023-01868-x.

Gross, M. R. (1951), Magnetic characteristics of non-magnetic metallic materials comparison of properties in strong and weak fields, Technical Report E.E.S. Report 4E(2)66904, U.S. Naval Engineering Experiment Station, Annapolis, Maryland, USA.

Hayt, W. H. & Buck, J. A. (2011), *Engineering Electromagnetics*, 8th edn, McGraw-Hill.

Ho, C. Y., Ackerman, M. W., Wu, K. Y., Havill, T. N., Bogaard, R. H., Matula, R. A., Oh, S. G. & James, H. M. (1983), 'Electrical resistivity of ten selected binary alloy systems', *Journal of Physical and Chemical Reference Data* **12**(2), 183–322.

Landau, L., Lifshitz, E. & Pitaevskii, L. (1984), *Electrodynamics of Continuous Media*, Course of Theoretical Physics, 2nd edn, Pergamon Press, Oxford, London, New York, Toronto, Sydney, Paris, Frankfurt.

Ledger, P. D. & Lionheart, W. R. B. (2015), 'Characterising the shape and material properties of hidden targets from magnetic induction data', *IMA Journal of Applied Mathematics* **80(6)**, 1776–1798.

Ledger, P. D. & Lionheart, W. R. B. (2018*a*), 'An explicit formula for the magnetic polarizability tensor for object characterization', *IEEE Transactions on Geoscience and Remote Sensing* **56(6)**, 3520–3533.

Ledger, P. D. & Lionheart, W. R. B. (2018*b*), 'Generalised magnetic polarizability tensors', *Mathematical Methods in the Applied Sciences* **41**, 3175–3196.

Ledger, P. D. & Lionheart, W. R. B. (2020), 'The spectral properties of the magnetic polarizability tensor for metallic object characterisation', *Mathematical Methods in the Applied Sciences* **43**, 78–113.

Ledger, P. D., Lionheart, W. R. B. & Amad, A. A. S. (2019), 'Characterisation of multiple conducting permeable objects in metal detection by polarizability tensors', *Mathematical Methods Applied Sciences* **42(3)**, 830–860.

Ledger, P. D., Wilson, B. A., Amad, A. A. S. & Lionheart, W. R. B. (2021), 'Identification of metallic objects using spectral magnetic polarizability tensor signatures: Object characterisation and invariants', *International Journal for Numerical Methods in Engineering* **122**, 3941–3984.

Ledger, P. D., Wilson, B. A. & Lionheart, W. R. B. (2022), 'Identification of metallic objects using spectral magnetic polarizability tensor signatures: Object classification', *International Journal for Numerical Methods in Engineering* **123**, 2076–2111.

Makkonen, J., Marsh, L. A., Vihonen, J., Järvi, A., Armitage, D. W., Visa, A. & Peyton, A. J. (2014), 'KNN classification of metallic targets using the magnetic polarizability tensor', *Measurement Science and Technology* **25**, 055105.

Makkonen, J., Marsh, L. A., Vihonen, J., Järvi, A., Armitage, D. W., Visa, A. & Peyton, A. J. (2015), 'Improving reliability for classification of metallic objects using a WTMD portal', *Measurement Science and Technology* **26**, 105103.

Marsh, L. A., Ktisis, C., Järvi, A., Armitage, D. W. & Peyton, A. J. (2013), 'Three-dimensional object location and inversion of the magnetic polarisability tensor at a single frequency using a walk-through metal detector', *Measurement Science and Technology* **24**, 045102.

Marsh, L. A., Ktistis, C., Järvi, A., .Armitage, D. W. & Peyton, A. J. (2014), 'Determination of the magnetic polarizability tensor and three dimensional object location for multiple objects using a walk-through metal detector', *Measurement Science and Technology* **25**, 055107.

NGSolve (n.d.), https://ngsolve.org. Accessed 12/10/2021.

O'Toole, M. D., Karimian, N. & Peyton, A. J. (2018), 'Classification of nonferrous metals using magnetic induction spectroscopy', *IEEE Transactions on Industrial Informatics* **14**(8), 3477–3485.

Özdeğer, T., Davidson, J. L., Ledger, P. D., Conniffe, D., Lionheart, W. R. B. & Peyton, A. J. (2023), 'Measuring the magnetic polarizability tensor of non-symmetrical objects', *IEEE Sensors Journal*. doi: 10.1109/JSEN.2023.3296439.

Özdeğer, T., Davidson, J. L., Van Verre, W., Marsh, L. A., Lionheart, W. R. B. & Peyton, A. J. (2021), 'Measuring the magnetic polarizability tensor using an axial multi-coil geometry', *IEEE Sensors Journal* **21**, 19322–19333.

Özdeğer, T., Ledger, P. D., Lionheart, W. R. B. & Peyton, A. J. (2022), 'Measurement of GMPT coefficients for improved object characterisation in metal detection', *IEEE Sensors Journal* **22(3)**, 2430–2446.

Özdeğer, T., Ledger, P. D. & Peyton, A. J. (2022), A study on the magnetic polarizability tensors of minimum metal anti-personnel landmines, *in* '2022 IEEE International Instrumentation and Measurement Technology Conference', IEEE, Ottawa, Canada, p. 21845853.

Schmidt, K., Sterz, O. & Hiptmair, R. (2008), 'Estimating the eddy-current modeling error', *IEEE Transactions on Magnetics* **44**(6), 686–689.

Schöberl, J. (1997), 'NETGEN - an advancing front 2D/3D-mesh generator based on abstract rules', *Computing and Visualization in Science* **1(1)**, 41–52.

Schöberl, J. (2014), C++11 implementation of finite elements in NGSolve, Technical report, ASC Report 30/2014, Institute for Analysis and Scientific Computing, Vienna University of Technology.

Schöberl, J. & Zaglmayr, S. (2005), 'High order Nédélec elements with local complete sequence properties', *COMPEL-The International Journal for Computation and Mathematics in Electrical and Electronic Engineering* **24(2)**, 374–384.

Schwab, C. & Suri, M. (1996), 'The p and hp versions of the finite element method for problems with boundary layers', *Mathematics of Computation* **65**, 1403–1429.

Wait, J. R. (1951), 'A conducting sphere in a time varying magnetic field', *Geophysics* **16(4)**, 666–672.

Westman, H. P., Karsh, M., Perugini, M. M. & Fujii, W. S., eds (1972), *Reference data for radio engineers*, 5th edn, Howard W. Sams & Co. Inc.

Whittington, C. & Rose, I. (2014), Nickel plating handbook, Technical report, Nickel Institute.

Williams, K. C., O'Toole, M. D. & Peyton, A. J. (2023), 'Scrap metal classification using magnetic induction spectroscopy and machine vision', *IEEE Transactions on Instrumentation and Measurement*. Early access.

Wilson, B. A. & Ledger, P. D. (2021), 'Efficient computation of the magnetic polarizability tensor spectral signature using POD', *International Journal for Numerical Methods in Engineering* **122**, 1940–1963.

Zaglmayr, S. (2006), High Order Finite Elements for Electromagnetic Field Computation, PhD thesis, Johannes Kepler University Linz.

Zhao, Y., Yin, W., Ktistis, C., Butterworth, D. & Peyton, A. J. (2014), 'On the low-frequency electromagnetic responses of in-line metal detectors to metal contaminants', *IEEE Transactions on Instrumentation and Measurement* **63**, 3181–3189.

Zhao, Y., Yin, W., Ktistis, C., Butterworth, D. & Peyton, A. J. (2016), 'Determining the electromagnetic polarizability tensors of metal objects during in-line scanning', *IEEE Transactions on Instrumentation and Measurement* **65**, 1172–1181.